OH and HO$_2$ radicals chemistry at a suburban site during the EXPLORE-YRD campaign in 2018

Xuefei Ma[1], Zhaofeng Tan[2], Keding Lu[1,*], Xinping Yang[1], Xiaorui Chen[1], Haichao Wang[1,3], Shiyi Chen[1], Xin Fang[1], Shule Li[1], Xin Li[1], Jingwei Liu[1], Ying Liu[1], Shengrong Lou[4], Wanyi Qiu[1], Hongli Wang[4], Limin Zeng[1], Yuanhang Zhang[1,5,6,*]

[1]State Key Joint Laboratory of Environmental Simulation and Pollution Control, College of Environmental Sciences and Engineering, Peking University, Beijing, China

[2]Institute of Energy and Climate Research, IEK-8: Troposphere, Forschungszentrum Juelich GmbH, Juelich, Germany

[3]School of Atmospheric Sciences, Sun Yat-sen University, Guangzhou, China

[4]State Environmental Protection Key Laboratory of Formation and Prevention of the Urban Air Complex, Shanghai Academy of Environmental Sciences, Shanghai, China

[5]Beijing Innovation Center for Engineering Sciences and Advanced Technology, Peking University, Beijing, China

[6]CAS Center for Excellence in Regional Atmospheric Environment, Chinese Academy of Science, Xiamen, China

Correspondence to: K. Lu (k.lu@pku.edu.cn), Y. Zhang (yhzhang@pku.edu.cn)

Abstract

The first OH and HO$_2$ radical observation in Yangtze River Delta, one of the four major urban agglomerations in China, was carried out at a suburban site Taizhou in summer 2018 from May to June, aiming to elucidate the atmospheric oxidation capacity in this region. The maximum diurnal averaged OH and HO$_2$ concentrations were 1.0×10^7 cm^{-3} and 1.1×10^9 cm^{-3}, respectively, which were the second highest HO$_x$ (sum of OH and HO$_2$) radical concentrations observed in China. HONO photolysis was the dominant radical primary source, accounting for 42% of the total radical initiation rate. Other contributions were from

27   carbonyl photolysis (including HCHO, 24%), O_3 photolysis (17%), alkenes ozonolysis (14%), and NO_3

28   oxidation (3%). A chemical box model based on RACM2-LIM1 mechanism could generally reproduce the

29   observed HO_x radicals, but systematic discrepancy remained in the afternoon for OH radical, when NO

30   mixing ratio was less than 0.3 ppb. Additional recycling mechanism equivalent to 100 ppt NO was capable

31   to fill the gap. The sum of monoterpenes was on average up to 0.4 ppb during daytime, which was allocated

32   all to α-pinene in the base model. Sensitivity test without monoterpene input showed the modelled OH and

33   HO_2 concentrations would increase by 7% and 4%, respectively, but modelled RO_2 concentration would

34   significantly decrease by 23%, indicating that monoterpene was an important precursor of RO_2 radicals in

35   this study. Consequently, the daily integrated net ozone production would reduce by 6.3 ppb if without

36   monoterpene input, proving the significant role of monoterpene on the photochemical O_3 production in this

37   study. Besides, the generally good agreement between observed and modelled HO_x concentrations suggested

38   no significant HO_2 heterogeneous uptake process during this campaign. Incorporation of HO_2 heterogeneous

39   uptake process would worsen the agreement between HO_x radical observation and simulation, and the

40   discrepancy would be beyond the measurement-model combined uncertainties using an effective uptake

41   coefficient of 0.2. Finally, the ozone production efficiency (OPE) was only 1.7 in this study, a few folds

42   lower than other studies in (sub)urban environments. The low OPE indicated slow radical propagation rate

43   and short chain length. As a consequence, ozone formation was suppressed by the low NO concentration in

44   this study.

1. Introduction

46   Stringent air quality regulations have been implemented in China for more than a decade to combat the

47   severe air pollution problems, and dramatically reduction of primary air pollutants such as sulfur dioxide

48   (SO_2), nitrogen oxides (NO_x), and coarse particulate matters (PM_{10}) has achieved. Besides, a significant

49   decrease in fine particulate matters ($PM_{2.5}$) is found since 2013, when the Chinese government took the

50   strictest measures to reduce the anthropogenic emission in the polluted regions (Wang et al., 2020b;Wang et

51   al., 2019b). However, the surface ozone (O_3) showed a contrasting trend with an increasing rate of 1-3 ppb

52   a^{-1} over the Chinese eastern megacity clusters, among which North China Plain and Yangtze River Delta

53   regions are of the most significant increase of 3-12 ppb a^{-1} (Wang et al., 2020b). The only known formation

54   pathway to O_3 in the troposphere is the photolysis of NO_2 (R1 and R2). The increasing O_3 despite the

55   successful reduction in NO_2 demonstrates the nonlinearity of the photochemistry caused by the dual role of

56   NO_x.

57    $NO_2 + hv \rightarrow NO + O(^3P)$ ($\lambda < 398$ nm)   (R1)

58    $O(^3P) + O_2 + M \rightarrow O_3 + M$ (R2)
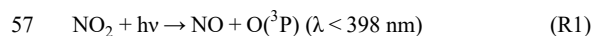
59   The ozone formation nonlinearity can be described by investigating HO_x radical chemistry (Tan et al.,

60   2018a;Tan et al., 2018b). In low NO_x conditions, the local ozone production rate $P(O_3)$ increases with NO_x

61   due to the efficient NO to NO_2 conversion by peroxy radicals (R3-R4). In high NO_x conditions, $P(O_3)$

62   decreases with NO_x because the radical termination (R5) overwhelms the radical propagation processes. The

63   key is to find the optimized reduction strategy for both NO_x and VOCs to efficiently control the O_3 production,

64   which the radical measurement could give insight to.

65    $HO_2 + NO \rightarrow OH + NO_2$ (R3)

66    $RO_2 + NO \rightarrow RO + NO_2$ (R4)

67    $OH + NO_2 \rightarrow HNO_3$ (R5)
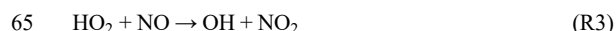
68   Numerous field campaigns focusing on the hydroxyl (OH) and hydroperoxy radical (HO_2) measurements

69   have been performed worldwide for the past decades, covering various environments including forest,

70   marine, remote, polar, rural, suburban, and urban (Stone et al., 2012). The measured OH concentrations

71   varied in an order of magnitude (in the range of 10^6-10^7 cm^{-3}) among different types of environments, and

72   the OH daily maximum concentrations showed a tendency of higher values in urban areas. Five field

73   campaigns have been implemented in China during summer periods, namely the Backgarden (2006), Heshan

74   (2014), Shenzhen (2018) campaigns in Pearl River Delta (PRD) (Lu et al., 2012;Tan et al., 2019a), and Yufa

75   (2006), Wangdu (2014) campaigns in North China Plain (NCP) (Lu et al., 2013;Tan et al., 2017;Wang et al.,

76   2019a) to investigate the atmospheric oxidation capacities and photochemistry characteristics of two of the

77   most polluted regions in China, in which Backgarden campaign reported the highest OH concentration

78   (15×10^6 cm^{-3}) ever observed (Lu et al., 2019). Chemical box model simulation based on conventional

79   mechanisms could generally reproduce the OH radical concentrations in these Chinese campaigns at NO

80   concentration above 1 ppb, but a tendency to underestimate OH radical are continuously observed at NO

81   concentration less than 1 ppb, which is a common feature in isoprene-rich forest environments and OH

82 concentration could be underestimated by a factor of up to 10 (Rohrer et al., 2014;Tan et al., 2001;Lelieveld

83 et al., 2008). Novel recycling mechanism related to isoprene and its degradation products without the

84 involvement of NO has been come up to be responsible for the OH measurement-model discrepancy in

85 isoprene-rich environments (Peeters et al., 2009;Peeters et al., 2014;Lelieveld et al., 2008), but it is not

86 sufficient to explain the large discrepancy for campaigns in urban and suburban environments. It was worth

87 noting that the high OH concentration might be caused by an unknown interference in OH measurements by

88 laser induced fluorescence (LIF) (Mao et al., 2012;Novelli et al., 2014;Hens et al., 2014;Feiner et al., 2016).

89 Mao et al. (2012) reported that up to 80% of OH measurement is interference in a pine forest. However, the

90 interference was minimal and within the instrumental detection limit in other campaigns under urban and

91 suburban environments by different LIF instruments (Griffith et al., 2016;Tan et al., 2017). Therefore, the

92 OH measurement accuracy need to be addressed prior to critical discussion about defects in our knowledge

93 of the radical chemistry.

94 Yangtze River Delta (YRD) region is one of the four major polluted regions in China and O_3 has become the

95 most critical pollutant in this region (Li et al., 2019). A four-year continuous observation showed the ozone

96 pollution days have been more than doubled from 2014 to 2017 (28 to 76 days) in YRD region (Liu et al.,

97 2020). Lu et al. (2018) reported that the monthly averaged daily maximum 8-h concentrations of O_3 were

98 even higher in YRD than in the NCP. Plenty of studies have been performed to investigate the ozone pollution

99 characteristics and diagnose the sensitivity of ozone formation to its precursors over this region (Zhang et

100 al., 2020;Ding et al., 2013;Tie et al., 2013;Geng et al., 2015;Xing et al., 2017), but none of the studies were

101 deployed with HO_x radical observations. In the present study, we report a new radical observation in YRD

102 region during the campaign EXPLORE-YRD (EXPeriment on the eLucidation of the atmospheric Oxidation

103 capacity and aerosol foRmation, and their Effects in Yangtze River Delta) together with a comprehensive set

104 of trace gases measurement. It provides a unique chance to investigate the photochemistry with the support

105 of HO_x radical observation in this region. Besides, the in-situ HO_x radical observation also allows to

106 investigate the impact of potential mechanisms such as HO_2 heterogeneous uptake on the photochemistry.

2. Methodology

2.1 Measurement site

109 The EXPLORE-YRD campaign was conducted in the summer of 2018 (14 May to 20 June) in the park of

110 meteorological radar station in suburban Taizhou (32.56˚N, 119.99˚E), Jiangsu Province, which is

111 approximately 200 km north-west and 100 km north-east of the two major megacities, Shanghai and Nanjing,

112 in Yangtze River Delta region (Fig. S1). The site was surrounded by fishponds and grass lands, featured with

113 strong biogenic emission and occasionally biomass burning. No major industrial emission was found within

114 500 meters. The closest road with slight traffic was about 100 meters to the South, and to the North and East

115 of the measurement site were the highway S28 and S35 with moderate traffic. For most of the campaign,

116 southerly and easterly winds prevailed, and brought air from the megacities and sea in upwind to this site

117 during the daytime. Thus, the sampled air mass during this campaign could generally embody the

118 atmospheric chemical characteristics in this region.

2.2 OH and HO$_2$ radical measurements

120 OH and HO$_2$ radicals were measured by the Peking University Laser Induced Fluorescence system (called

121 PKU-LIF), which was successfully deployed for several times in previous campaigns in Pearl River Delta

122 and North China Plain regions in China (Tan et al., 2017;Tan et al., 2018c;Tan et al., 2019a;Ma et al., 2019).

123 OH radical is detected by laser-induced fluorescence at a low pressure cell (4 hPa) after a sampling nozzle

124 (Hofzumahaus et al., 1998;Holland et al., 2003). The OH signal is determined by tuning the laser wavelength

125 (308 nm) on- and off-line, so called wavelength modulation. Specific description of the instrument

126 configuration could be found in (Tan et al., 2017) and references therein.

127 HO$_2$ radical is chemically converted to OH by reaction with NO that is injected into the flow through a ring-

128 shaped injector installed below the sampling nozzle and then is detected in the form of OH in the second

129 detection cell. The added maximum NO mixing ratio was chosen to be 5 ppm, resulting in the maximum

130 HO$_2$ conversion efficiency to be 20%. Furthermore, the NO injection was set to be switched between 2.5

131 ppm and 5 ppm every 2 minutes, and any significant RO$_2$ interference will differ the HO$_2$ measurement

132 between two NO injection modes. It turned out that potential interference from RO$_2$ radical was well within

133   the HO_2 measurement uncertainty (13%) during this campaign.

134   The PKU-LIF instrument was calibrated every 2 days during the campaign using a radical calibration source

135   (Hofzumahaus et al., 1996;Holland et al., 1998). Stable sensitivities were found over the whole campaign

136   with reproducibility of 1.2% and 8.0% for OH and HO_2, respectively (1σ standard deviation). Thus, averaged

137   sensitivity was applied for the radical concentration determination. Considering the combined uncertainty of

138   calibration source (10%, 1σ) with reproducibility of calibrated sensitivities, the accuracies of OH and HO_2

139   measurement were 10% and 13%, respectively.

140   Previous studies indicated OH measurements by Laser Induced Fluorescence technique using wavelength

141   modulation might suffer from unknown internal-produced interference (Mao et al., 2012;Novelli et al., 2017).

142   To investigate possible OH interference, we performed an extended chemical modulation experiment on 7

143   June. A chemical modulation device consisting of a flowtube was placed in front of the OH sampling nozzle,

144   with which ambient OH was scavenged by adding propane. During the experiment, nitrogen and propane

145   was added alternatively for every 5 minutes to deduce the unexplained OH signals from adjacent

146   measurement modes. A description of the prototype chemical-modulation reactor used with PKU-LIF is

147   given by Tan et al. (2017).

148   **2.3 Trace gases measurements**

149   A large number of trace gases and aerosol properties related to the atmospheric oxidation chemistry

150   investigation were measured simultaneously. Instruments were placed in sea-containers with their sampling

151   inlets mounted 5 meters above ground. The detail of instrumentation is described by (Wang et al., 2020a).

152   In Table 1, the measured species related to photochemistry study are listed together with the performance of

153   instruments.

154   O_3, NO, NO_2, SO_2 and CO were detected by a series of commercial analyzers from Thermo Inc. O_3 was

155   measured by a UV Photometric analyzer (Model 49i). Both NO and NO_2 were measured by a trace-level

156   analyzer (Model 42i) using chemiluminescence method. Therein, NO_2 measurement was accomplished by a

157   home-built photolytic converter to avoid interference from other NO_y species. HONO measurement was

158   deployed by a Long-path Absorption Photometry with the time resolution of 1 min. A gas chromatograph

159   coupled with a flame ionization detector and mass spectrometer (GC-FID-MS) was deployed to measure

160 volatile organic compounds (VOC) including non-methane hydrocarbons (C2-C11 alkanes, C2-C6 alkenes,

161 C6-C10 aromatics, isoprene, sum of monoterpenes), and oxygenated VOCs including methyl vinyl ketone

162 (MVK)/Methacrolein (MACR), methyl-ethyl-ketone (MEK), acetaldehyde (ACD), acetone (ACT) in a time

163 resolution of 1 hour. The sum of monoterpenes was also detected by proton transfer reaction mass

164 spectrometry (PTR-MS). Formaldehyde and glyoxal were measured by a commercial and a home-built

165 instruments, namely Hantzsch and CEAS, respectively. Additionally, meteorological parameters including

166 temperature, relative humidity, pressure, wind speed, and wind direction were all measured simultaneously.

167 Photolysis Frequencies was calculated by integrated actinic flux measured by a spectroradiometer.

168 **2.4 Model description**

169 An observation-constrained box model based on RACM2-LIM1 mechanism (Goliff et al., 2013;Peeters et

170 al., 2014) was used to simulate the OH and HO_2 radical concentrations. Briefly, observations of the

171 photolysis frequencies, O_3, NO, NO_2, CO, CH_4, SO_2, HONO, C2-C12 VOCs, and certain oxygenated VOCs

172 such as HCHO, acetaldehyde, glyoxal and acetone as well as the meteorological parameters were used to

173 constrain the model with a time resolution of 5 min. The organic compounds were not treated individually

174 but assigned to different lumped species according to the reactivities with OH. The classification of the

175 constrained organic compounds in RACM2 were listed in Table 2 in detail. The sum of monoterpene is

176 allocated to α-pinene in the model and the uncertainty due to such simplification is discussed in section 4.2.2.

177 Isomerization of isoprene-derived peroxy radicals were also considered. Other lumped secondary species

178 were unconstrained due to the technical limits but generated numerically by the model calculation.

179 Additional first-order loss term equivalent to a lifetime of 8 hours was given to all species to represent

180 physical losses by means of deposition, convection, and advection. The observed-to-model of PAN is 1.09

181 using this physical loss rate. According to the Monte-Carlo simulation tests, the estimated 1σ uncertainty of

182 the model calculation was 32% and 40% for OH and HO_2, respectively, arising mainly from the uncertainties

183 of both observational constraints and kinetic rate constants, among which the rate constant between HO_2 and

184 NO, dilution time and NO concentration were of most significant importance in this study.

Atmospheric
Chemistry
and Physics
Discussions

3. Results

3.1 Meteorological and chemical conditions

The meteorological condition encountered during the campaign was characterized by high temperature (up to 35 °C), high relative humidity (54% on average) and strong solar radiation. The wind speed was usually below 2 m s^{-1} during the daytime. Back trajectory analysis demonstrated that the air masses were predominately transported from the South and East during the campaign. High O_3 concentrations were frequently observed on days when the air masses transported to the measurement site had passed through the South especially the Southwest large city clusters. As shown in Fig. 1, the daytime O_3 concentrations exceeded the Chinese national air quality standard level II (hourly averaged limit 93 ppb) on several days and reached as high as 150 ppb on 5 and 6 June.

Figure 2 shows mean diurnal profiles of the key parameter observations. The averaged period is selected when HO_x measurements were available (23 May-17 June excluding the break). Solar radiation was intense during the whole campaign indicated by photolysis frequencies $j(O^1D)$ and $j(NO_2)$. NO concentration peaked at 4 ppb during morning rush hour and then dropped to 0.2 ppb at noon. O_3 concentration started to increase after sunrise and reached the peak of 86 ppb around noon and lasted until sunset. Subsequently, O_3 concentration decreased and partially converted to NO_2 due to the absence of sunlight. The total oxidant (O_x), the sum of O_3 and NO_2 also decreased after sunset. Along with the increased NO_2 at night, HONO concentration increased and reached the maximum of up to 1.3 ppb at sunrise and then declined rapidly due to the fast photolysis. The averaged HONO concentration was 0.6 ppb on the daytime basis. Peroxyacyl nitrates (PAN) is an indicator for active photochemistry which increased since sunrise reaching maximum of 1.6 ppb at 12:00 and then decreased in late afternoon during this campaign. However, other oxidation products, including HCHO and glyoxal, similar to CO and SO_2, peaked at 8:00 CNST rather than in the noon and late afternoon and decreased afterwards, indicating an anthropogenic emission-related origin of these species.

Isoprene showed a broad peak of 0.2 ppb from 09:00 to 15:00, which was several times lower than during the previous summer campaigns (Lu et al., 2012;Lu et al., 2013;Tan et al., 2017). The sum of monoterpene concentrations varied from 0.2 ppb to 0.4 ppb showing a diurnal peak around noon. Though the speciation

212 is not known, the daytime monoterpene concentration was comparable to monoterpene dominated pine forest

213 (Kim et al., 2013;Hens et al., 2014). The role of monoterpene to HO_x chemistry is discussed in section 4.2.2.

3.2 OH and HO_2 radical observation

215 Figure 3 shows the timeseries of the observed and calculated OH and HO_2 radical concentrations. Continuous

216 measurement of HO_x radicals was interrupted by the rainfalls and calibration or instrument maintenance.

217 Distinct diurnal variation was observed for both OH and HO_2 radical. The daily maxima of OH and HO_2

218 concentration were in the range of $(8-24)\times10^6$ cm^{-3} and $(4-28)\times10^8$ cm^{-3}, respectively. The mean diurnal

219 profiles showed that averaged OH and HO_2 peak concentrations (1-h averaged) were 1.0×10^7 cm^{-3} and

220 1.1×10^9 cm^{-3}, respectively (Fig. 4). Additionally, the chemical modulation tests performed on 7 June, an O_3

221 polluted day, indicated the unknown OH interference, if existed, was insignificant and below the detection

222 limits during this campaign (Fig. S2).

223 For comparison, the daytime measured OH concentration in this campaign together with the OH

224 concentrations in Yufa and Wangdu campaigns in NCP region and in Backgarden, Heshan and Shenzhen

225 campaigns in PRD region, where OH radical observations were available in China were summarized in Table

226 3 and Figure 5. Overall, the OH radical concentration at present study was relatively higher than during other

227 campaigns except for the Backgarden campaign in 2006 (Hofzumahaus et al., 2009). It demonstrated the

228 strong atmospheric oxidation capacity in this region among the three megapolitan areas (NCP, PRD, and

229 YRD) in China from the perspective of OH concentration.

230 We also found strong correlation between observed OH radical concentration and photolysis frequency

231 $(j(O^1D))$ during the EXPLORE-YRD campaign, with the correlation coefficient R^2 and the correlation slope

232 being 0.85 and 4.8×10^{11} s cm^{-3}, respectively (Fig. 6). Notably, the slopes were in the range of $(4.0-4.8)\times10^{11}$

233 s cm^{-3} for all the previous filed campaigns in NCP and PRD regions, for both summer and winter (Tan et al.,

234 2017;Tan et al., 2018c;Lu et al., 2012;Ma et al., 2019). It suggested that the atmospheric oxidation capacity

235 to sustain the radical concentrations was comparable under various chemical conditions in the three major

236 urban agglomerations. Besides, the intercept of the linear fit for this campaign was about 7.6×10^5 cm^{-3}, which

237 was comparable to the Wangdu campaign in 2014 (7.7×10^5 cm^{-3}) and lower than the Yufa and Backgarden

238 campaigns in 2006 (1.6×10^6 cm^{-3} and 2.4×10^6 cm^{-3}, respectively). It represented the non-photolytically

239 produced OH concentration.

3.3 Modelled OH reactivity

241 OH reactivity (k_{OH}) is the inverse of OH radical lifetime and could be defined by the sum of the OH reactants

242 concentrations multiplied by its reaction rate constant versus OH radical (Eq. 1) (Fuchs et al., 2017;Yang et

243 al., 2016;Yang et al., 2019;Lou et al., 2010).

244 $k_{OH} = \sum_i k_{OH+X_i} [X_i]$ (Eq. 1)

245 In this study, OH reactivity is calculated from the measured compounds and modelled secondary species.

246 The modelled OH reactivity varied from 5 s^{-1} to 40 s^{-1} (Fig. 3).

247 The typical diurnal variation of k_{OH} showed a peak in the morning with enhanced contribution from NO$_x$ and

248 dropped to the minima in the afternoon (Fig. 7a). The averaged k_{OH} for periods with OH radical measurement

249 was 10.8 s^{-1} on daytime basis (08:00-16:00), and a total of 36% of the calculated k_{OH} could be attributed to

250 the inorganic compounds (Fig. 7b). Measured VOC species contributed 42% of k_{OH} including primary VOCs

251 and part of oxygenated ones. On average, the measured OVOCs including HCHO and other OVOCs listed

252 in Table 2 constituted 18% of the k_{OH}. The remaining 22% of k_{OH} is contributed by the model generated

253 species, which was comparable to the measured OVOCs.

4. Discussion

4.1 Sources and sinks of RO$_x$ radicals

256 The sum of OH, HO$_2$, and RO$_2$ radicals are known as RO$_x$ radical. The interconversion within the RO$_x$ radical

257 family is relatively efficient via radical propagation reactions, in which the number of consumed and

258 produced radicals are equal and do not change the total RO$_x$ concentrations. In this section, we concentrate

259 on the radical initiation processes that produce radicals from non-radical molecules, and chain termination

260 processes that destroy radicals. The radical primary production consists of photolysis reactions and alkene

261 ozonolysis. Radical termination processes include reactions with nitrogen oxides and recombination of

262 peroxy radicals.

263 Figure 8 presents the mean diurnal profiles of RO$_x$ radical production and destruction rates based on the

264 model calculation. The P(RO$_x$) and L(RO$_x$) show distinct diurnal variation with maximum of 6.8 ppb h^{-1} at

265   noontime. In other campaigns, diurnal maximum $P(RO_x)$ varies from 1.1 ppb h^{-1} at a suburban site in

266   Nashville to about 11.6 ppb h^{-1} at a rural site near London during a heatwave. The $P(RO_x)$ in EXPLORE-

267   YRD campaign is comparable to those found in Mexico 2003, Mexico 2006 and Yufa 2006 (Table 3).

268   The daytime averaged radical chemistry production rate was 5.7 ppb h^{-1}, of which 83% was attributed to

269   photolytic process. HONO photolysis was the dominant primary source for the entire day and contributed

270   up to 42% of $P(RO_x)$ on daytime basis. The photolysis of HONO is one of the most important radical primary

271   sources in both urban and suburban areas (Ren et al., 2003b;Dusanter et al., 2009b;Michoud et al.,

272   2012;Whalley et al., 2018;Tan et al., 2017). Besides, carbonyl compounds (including HCHO) photolysis was

273   also an important contributor to radical primary source under urban and suburban condition (Kanaya et al.,

274   2007;Griffith et al., 2016;Emmerson et al., 2007). In this study, carbonyl compounds photolysis accounted

275   for on average 24% of $P(RO_x)$, in which 14% was from HCHO solely. The dominant primary radical source

276   in remote regions, ozone photolysis (generating O^1D and subsequently reacts with H_2O to produce OH), also

277   played a significant role in this study, contributing 17% to $P(RO_x)$. Besides, the non-photolytic radical source

278   alkene ozonolysis peaked at around 10:00 in the morning, and the most important O_3 reactant was

279   monoterpene (35% on daytime basis). It was worth noting that $P(RO_x)$ reduced significantly after sunset

280   while there was a small peak of 1.5 ppb h^{-1} appeared at dusk. The nighttime radical chemistry was mainly

281   initiated by NO_3 oxidation (82%) with monoterpene in the first half of the night, but the NO_3 chemistry was

282   suppressed from midnight to sunrise by the increasing NO concentration because of the efficient titration

283   effect (Wang et al., 2020a).

284   During the EXPLORE-YRD campaign, the RO_x termination processes were mainly dominated by the

285   OH+NO_2 reaction before 08:00 and by peroxy radical self-reaction in the afternoon (Fig. 8). On daytime

286   basis, nitrate formation and peroxy radical recombination both accounted for half of $L(RO_x)$. The peroxy

287   radical recombination including HO_2+RO_2, HO_2+HO_2, and RO_2+RO_2 reactions contributed 33%, 15%, and

288   1% to $L(RO_x)$, respectively. Because the HO_2 and RO_2 concentrations were usually similar, the different

289   contributions between three kinds of peroxy radical recombination were caused by different reaction rate

290   constants. In RACM2, the HO_2+RO_2 reaction rate varied from 5.1×10^{-12} cm^3 molecule^{-1} s^{-1} (methyl peroxy

291   radical at 298 K) to 1.6×10^{-11} cm^3 molecule^{-1} s^{-1} (isoprene derived RO_2 at 298K). In comparison, the effective

292   HO_2+HO_2 reaction rate constant was 3.5×10^{-12} cm^3 molecule^{-1} s^{-1} assuming ambient H_2O mixing ratio of 2%.

293   The self-combination of methyl peroxy radicals rate constant was 3.5×10^{-13} cm^3 $molecule^{-1}$ s^{-1}, one order of

294   magnitude smaller than the other radical recombination reaction. The reversible reaction between peroxyacyl

295   radical and PANs became a net radical sink in the morning because relatively high-NO_2 and low-temperature

296   shifted the thermodynamic equilibrium to form PANs. The net formation of PANs followed by physical

297   losses contributed on average 12% of $L(RO_x)$. Besides, part of the RO_2 species react with NO to form organic

298   nitrate rather than recycle to HO_2 radical, resulting in 6% of the radical losses during the daytime. As for the

299   nighttime, since the radicals formed from NO_3 oxidation were dominantly OLND and OLNN in RACM2,

300   the nighttime radical losses were dominated by the formation of organic nitrates from OLND and OLNN

301   reaction with themselves and other peroxy radicals.

302   **4.2 OH and HO_2 measurement-model comparison**

303   OH and HO_2 radical concentrations were simulated by a box model, which showed good agreement with

304   observation (Fig. 3). A significant discrepancy between observed and modelled HO_2 concentrations occurred

305   on 12 and 13 June. On these two days, maximum HO_2 increased to 2.6×10^9 cm^{-3}, twice of the campaign

306   averaged maximum, while modelled HO_2 concentration remained nearly the same. We investigated the

307   discrepancy between observed and modelled HO_2 against different chemical composition but could not

308   identify the cause of elevated HO_2 concentration on these two days. In the following analysis, the

309   observation-model comparison is focus on the mean diurnal average to extract the overall feature of the

310   campaign.

311   **4.2.1 OH underestimation in low NO regime**

312   As shown in Fig. 4, the modelled OH concentration captured the increasing trend in the morning but

313   unpredicted the measurement since 10:00 with largest discrepancy occurred at noon. The HO_2 measurement-

314   model comparison showed similar diurnal variation but the largest discrepancy shifted to 1 hour later

315   together with diurnal maximum. On daytime basis, the modelled OH and HO_2 radical concentrations were

316   on average 30% and 28% smaller than measurements, respectively. The discrepancies can be explained by

317   combining 1σ uncertainties (10% and 13% for measurement and 32% and 40% for model calculation). In

318   fact, the HO_2 discrepancy in the mean diurnal profile was mainly caused by two outlier days, which

Atmospheric
Chemistry
and Physics
Discussions
Open Access
EGU

319   disappeared in the median diurnal profile (Fig. S3). However, the discrepancy of OH was also observed in

320   median diurnal profile indicating a persistent OH underestimation during afternoon.

321   The OH underestimation discrepancy showed dependence on the NO concentration. Figure 9 illustrates the

322   dependence of observed and modelled HO_x radicals on NO concentration. To remove the influence of

323   photolysis on OH radical, OH concentration was normalized to $j(O^1D)$ prior to NO dependence analysis.

324   The observed median OH_{norm} was almost constant over the whole NO regime, while the modelled value

325   tended to decrease towards lower NO (<0.3 ppb). The modelled OH_{norm} was 42% smaller than the observed

326   one at NO mixing ratio below 0.1 ppb (Fig. 9), which was beyond the measurement-model combined

327   uncertainty. This discrepancy was mainly caused by the data obtained in the afternoon. The observed and

328   modelled HO_2 agreed throughout the NO regime (Fig. 9), and was consistent with the median diurnal profiles.

329   Such OH-underestimation in low NO regime (typically with NO concentration less than 1 ppb) was

330   frequently found in environments with intense biogenic emission, especially isoprene (Tan et al., 2001;Ren

331   et al., 2008;Lelieveld et al., 2008;Whalley et al., 2011;Stone et al., 2011;Lu et al., 2012;Hofzumahaus et al.,

332   2009;Lu et al., 2013). We included up-to-date chemical mechanisms related to H-shift processes to consider

333   the impact of additional OH source, such as the H-shift mechanism of isoprene derived peroxy radicals

334   (Peeters et al., 2014). However, during this campaign, isoprene concentration was only 0.2 ppb contributing

335   5% of the modelled OH reactivity and thus play a minor role in OH chemistry. Therefore, other process

336   should account for the OH underestimation in low NO condition.

337   To resolve the OH underestimation, a genetic mechanism X was proposed for the Backgarden 2006 campaign,

338   in which X served as NO that converted RO_2 to HO_2 and then HO_2 to OH (Hofzumahaus et al., 2009).

339   Sensitivity tests demonstrated the requested amount of X was equivalent to 100 ppt NO for the EXPLORE-

340   YRD campaign (Fig. 9). Comparatively, the X concentration is the same as in Wangdu campaign (Tan et al.,

341   2017) but smaller than those identified in Backgarden (0.8 ppb (Hofzumahaus et al., 2009)) , Yufa (0.4 ppb

342   (Lu et al., 2013)), and Heshan (0.4 ppb (Tan et al., 2019a)), where the biogenic isoprene and OH reactivities

343   were three to five times and twice as high as during this campaign, respectively (Table 3). It should also be

344   pointed out that the precedingly quantified X of 100 ppt equivalent NO was supposed to be the lowest limit

345   in this study, if missing reactivity existed. On the other hand, the OH measurement-model discrepancy could

346   be attributed to measurement artifacts (Mao et al., 2012;Novelli et al., 2014;Rickly and Stevens, 2018),

347   although there is no hint for significant OH measurement interference during the EXPLORE-YRD campaign.

348   However, one should note that the precision is not good enough to rule out the possibility.

4.2.2 Monoterpenes influence

350   The observed monoterpenes varied from 0.2 to 0.4 ppb showing a broad peak around noon (Fig. 2). The high

351   monoterpene concentration and daytime peak indicate a strong daytime source given its short lifetime due

352   to oxidation (24 minutes for α-pinene or 8.2 minutes for Limonene, OH=1.0×10^7 cm^{-3}, O$_3$=80 ppb). The

353   diurnal variation was different from forest environments where maxima usually appeared at night (Kim et

354   al., 2013;Wolfe et al., 2014;Hens et al., 2014). The relatively low nighttime monoterpenes could be related

355   the strong NO$_3$ chemistry in this study (Wang et al., 2020a).

356   In the base model run, observed monoterpenes concentrations were all allocated to α-pinene in the model

357   accounting for 0.5 s^{-1} of k_{OH} (Fig. 7). A sensitivity test without monoterpenes constrained showed the k_{OH}

358   decreased by 1.0 s^{-1}, half of which was accounted from degradation products of α-pinene. Consequently, the

359   daytime OH and HO$_2$ concentrations increased by 7% (5×10^5 cm^{-3}) and 4% (3×10^7 cm^{-3}), respectively (Fig.

360   4).

361   To investigate the uncertainty of unknown monoterpenes speciation, we performed a sensitivity test to

362   attribute the sum of monoterpenes to Limonene, another monoterpene species in RACM2. In this case, the

363   OH concentration decreased by 11%, while the HO$_2$ concentration slightly increased by 1% relative to the

364   base case. The reduced modelled OH concentration was resulted from the three times faster reaction rate

365   constant of Limonene with OH (1.6×10^{-10} cm^{-3} s^{-1} at 298K) than that of α-pinene (5.3×10^{-11} cm^{-3} s^{-1} at 298K).

366   Other studies conducted in forested environments with strong influence of monoterpenes from pine trees

367   emission found discrepancies of up to three times in HO$_2$ measurement-model comparison (Kim et al.,

368   2013;Wolfe et al., 2014;Hens et al., 2014). In the present study, however, OH and HO$_2$ concentrations were

369   reproduced by chemical model within combined uncertainty during daytime with relatively high

370   monoterpenes concentrations suggesting that no significant missing process in the current mechanisms.

371   Sensitivity tests also indicated that the different assumptions of monoterpenes speciation had minor impact

372   on modelled OH and HO$_2$ concentrations (about 10%). Thus, our results demonstrated that the monoterpene

373   oxidation chemistry in the environments with both anthropogenic and biogenic influence can be captured by

374   the applied chemical mechanisms with respect of HO_x concentration.

4.2.3 HO₂ heterogenous uptake

376   A recent model study proposed that HO_2 heterogeneous uptake processes play an important role in HO_x

377   radical chemistry and thus suppress ozone formation in China (Li et al., 2019). The RACM2-LIM1

378   mechanisms used in our study only consist gas phase reactions without heterogeneous chemistry. Therefore,

379   in this section, we performed a sensitivity test with HO_2 radical uptake considered to investigate the potential

380   impact on the modelled radical concentrations by adding a radical termination process (R6).

381   HO_2 + Aerosol → products   (R6)
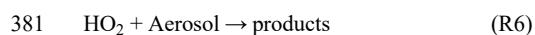
382   The heterogeneous loss rate of HO_2 radical is limited by the free molecular collision because the aerosol

383   surface is mainly contributed by submicron particles. HO_2 radical uptake process can be simplified as a

384   pseudo first order reaction, and the first-order kinetics constant can be calculated by the Eq. 2:

385    $k_{HO_2} = \frac{V_{HO_2} \times S_a \times \gamma}{4}$ (Eq. 2)

386    $V_{HO_2} = \sqrt{\frac{8RT}{\pi \times 0.033}}$ (Eq. 3)

387   V_{HO2} represents the mean molecular velocity of HO_2 determined by Eq. 3. S_a is the humid aerosol surface

388   areas calculated by the SMPS measured particle number and size distribution in each size bin corrected by

389   the hygroscopic growth factor. γ is the effective HO_2 uptake coefficient on aerosol giving the probability of

390   HO_2 loss by impacting the aerosol surface.

391   The effective uptake coefficients vary from 10^{-5} to unity from multiple laboratory studies (Thornton et al.,

392   2008;Taketani et al., 2009;Taketani and Kanaya, 2010;George et al., 2013;Lakey et al., 2015;Zou et al.,

393   2019). A relatively high value of 0.2 was found in aerosol samples collected in North China Plain, which

394   was attributed to the abundant dissolved copper ions in aqueous aerosol (Taketani et al., 2012). A study based

395   on radical experimental budget analysis determined the effective HO_2 uptake coefficient to be 0.08±0.13 in

396   North China Plain (Tan et al., 2020). In our sensitivity tests, both coefficients were applied and simulated

397   separately.

398   As shown in Fig. 4, the incorporation of HO_2 heterogeneous uptake process worsened the model-

399   measurement agreement with both OH and HO_2 radicals for both cases. In fact, the agreements between

400   measurement and model calculation of OH and HO_2 indicated that the base model without heterogenous

401   reaction captured the key process for OH and HO_2 radical chemistry in this study. The modelled OH and

402   HO_2 radicals were reduced by 10% and 20%, respectively, for the coefficient of 0.2, and by 5% and 10% for

403   the coefficient of 0.08. For the case the coefficient of 0.08, the increased radical loss rate from HO_2 uptake

404   process was 0.4 ppb h^{-1} on daytime basis, which was smaller than that during the Wangdu campaign (0.6±1.3

405   ppb h^{-1}). The discrepancy between two studies was caused by the lower aerosol surface areas during the

406   EXPLORE-YRD campaign (750 compared to 1600 μm^2 cm^{-3}). The measured and modelled HO_2

407   concentrations agreed within 33% on daytime basis, which was less than the 40% uncertainty of HO_2

408   simulation. However, this discrepancy enlarged to 51% as the coefficient increased to 0.2 exceeding the

409   uncertainty of HO_2 simulation. Though we could not rule out the HO_2 heterogeneous loss, the model

410   sensitivity tests suggested that HO_2 uptake coefficient should be less than 0.2, if the HO_2 heterogeneous loss

411   played a role during this campaign.

412   **4.3 local Ozone production rate**

413   Peroxy radical chemistry is intimately tied to the atmospheric ozone production. All peroxy radicals which

414   could react with NO to form NO_2 leading to ozone formation ($F(O_x)$), as expressed in Eq. 4. In this study,

415   the ozone formation contributing from RO_2 was derived from model calculation due to the absence of RO_2

416   measurement. The reaction rate constant between HO_2 and NO is approximately 8.5×10^{-12} cm^3 molecule^{-1} s^{-1}

417   at 298 K, while the rate constant for the reaction of RO_2 with NO varies significantly (ranging in fivefold)

418   depends on the specific speciation in RACM2. Besides, the NO_2 yield from RO_2 and NO reaction also differs

419   for different RO_2 groups in RACM2. Part of the RO_2 radicals reacts with NO forming organic nitrates rather

420   than producing NO_2 and recycling the peroxy radicals. The nitrate yield increases with higher carbon

421   numbers and branch structure. Therefore, the NO_2 production from RO_2+NO reaction is manipulated by the

422   effective reaction rate considering both reaction rate constant and NO_2 yield for different RO_2 species (Eq.

423   4).

424    $F(O_x) = k_{HO_2+NO} [HO_2] [NO] + \sum_i k_{RO_2i+NO} [RO_2]_i [NO]$ (Eq. 4)

425   On the other hand, formed O_3 could be involved and consumed in the radical chain reactions by initiating

426   the radicals from photolysis and reaction with alkenes and propagating the radicals from reaction with OH

427 and HO_2, and besides, part of the NO_2 would react with OH to generate nitric acid rather than photolysis

428 ($L(O_x)$). Additionally, NO_2 could also react with O_3 to form NO_3 radical, which could further combine with

429 another NO_2 to form N_2O_5 or oxidize VOCs to form organic nitrates, leading to 2 to 3 times faster O_x loss

430 than NO_3 radical formation. Considering the fact that NO_3 radical could be easily photolyzed to regenerate

431 NO_2 and O_3 or be titrated by NO to regenerate NO_2, the contribution from net NO_3 radical formation pathway

432 was taken into account by taking the largest O_x loss per NO_3 net formation of 3 in Eq. 5.

433 $L(O_x) = J(O^1D) [O_3] \times \varphi + k_{O_3+Alkenes} [Alkenes] [O_3] + k_{O_3+OH} [OH] [O_3] + k_{O_3+HO_2} [HO_2] [O_3] +$

434 $k_{OH+NO_2} [OH] [NO_2] + 3 \times (k_{NO_2+O_3} [NO_2] [O_3] - k_{NO+NO_3} [NO] [NO_3] - j_{NO_3} [NO_3])$ (Eq. 5)

435 Thus, the net ozone production rate ($P(O_x)$) could be deduced from the difference between O_x formation and

436 O_x loss rates as expressed in Eq. 6.

437 $P(O_x) = F(O_x) - L(O_x)$ (Eq. 6)

438 Figure 10a shows the mean diurnal profiles of the calculated $F(O_x)$ and $L(O_x)$ in this study. Fast ozone

439 formation rate of up to 20 ppb h^{-1} was observed at 09:00, while the maximum ozone loss rate of 4 ppb h^{-1}

440 shifted to two hours later at noon, when the ozone formation rate reduced to 11.4 ppb h^{-1}. This rate was

441 comparable to other campaigns conducted in rural areas, while the ozone production rates increased

442 significantly in urban areas, where the noontime ozone formation rates varied from 13.9 ppb h^{-1} in Tokyo to

443 65 ppb h^{-1} in Mexico (Table 3).

444 Fast ozone formation is the consequence of both strong primary source and efficient radical propagation.

445 The latter one can be evaluated by the ratio between $F(O_x)$ and $P(RO_x)$ and known as ozone production

446 efficiency (OPE). As discussed in Sect. 4.1, the radical primary source was relatively high during the

447 EXPLORE-YRD campaign, and thus, the OPE was only 1.7, which was smaller than or comparable to other

448 rural campaigns (Table 3). Urban campaigns in US, Mexico and Tokyo showed significant higher OPE

449 varying from 6 to 10 (Table 3) probably benefit from the moderate NO_x level. In comparison, OPE was

450 smaller in four megacities in China (Beijing: 3.4, Shanghai: 3.1, Guangzhou: 2.2, Chongqing: 3.6) than in

451 US cities ranging from 3 to 7 because the suppression of high NO_x in Chinese cities (Tan et al., 2019b).

452 However, during the EXPLORE-YRD campaign, the low OPE indicates that the radical propagation chain

453 length was relatively short due to low NO conditions.

454 As shown in Fig. 10b, the integrated net ozone production was 68.3 ppb d^{-1} over the entire daytime (08:00-

455 16:00). The daily integrated P(O$_x$) calculated based on the modelled peroxy radicals was 6.9 ppb lower than

456 on derived from observation (Fig. 10b). The discrepancy for observation and model derived P(O$_x$) mainly

457 appears at NO concentration larger than 1 ppb (Fig. 9).

458 We also investigated the impact of different model scenarios on P(O$_x$) by comparing integrated P(O$_x$) in

459 different cases to that obtained in base model (Fig. 10b). Sensitivity test without α-pinene constrained

460 predicted 6.3 ppb less daily integrated net ozone production than base case. Meanwhile, the contribution of

461 α-pinene derived peroxy radicals (APIP) on F(O$_x$) only accounted for 2.3 ppb O$_3$ formation (Fig. 10a). The

462 difference can be attributed to the degradation products of α-pinene which also contribute to ozone

463 production. For example, aldehyde (ALD) is an important daughter product from α-pinene oxidation, which

464 reacts with OH and forms acyl peroxy radicals. Acyl peroxy radicals have two advantages in ozone formation.

465 On one hand, acyl peroxy radicals have the fastest rate constants with NO among all the peroxy radicals

466 (2~5 times faster than others). On the other hand, acyl peroxy radicals react with NO to produce NO$_2$ and

467 methyl or ethyl peroxy radicals, which can further oxidize the NO to NO$_2$ and generate HO$_2$. Given that the

468 modelled HO$_2$ concentration increased by 4% in the sensitivity test, the smaller in P(O$_x$) was mainly

469 attributed to significant reduction in modelled RO$_2$ concentration. In fact, the modelled RO$_2$ concentration

470 would reduce by 23% if α-pinene is not constrained to observation, which indicates α-pinene is an important

471 RO$_2$ precursors. It proves that monoterpene contributes significantly to the photochemical production of O$_3$

472 in this study.

473 Additional HO$_2$ heterogeneous uptake process in the model run would reduce the daily net O$_3$ production by

474 4.8 ppb by assuming the effective coefficient of 0.08. The reduction in P(O$_x$) was only slightly smaller than

475 the relative change in modelled HO$_2$ concentration (10%) because 62% of the F(O$_x$) was contributed by the

476 reaction of HO$_2$ with NO (Fig. 10a).

477 **4   Conclusion**

478 A comprehensive filed campaign to elucidate the atmospheric oxidation capacity in Yangtze River Delta in

479 China was carried out in summer 2018, providing the first OH and HO$_2$ radicals observations in this region.

480 Daily maximum concentrations of OH and HO$_2$ radicals were in the range from 8 to 24×10^6 cm^{-3} and 4 to

481 28×10^8 cm^{-3}, with mean values of 1.0×10^7 cm^{-3} and 1.1×10^9 cm^{-3}, respectively. The OH radical was of the

482 second highest concentration among the observations in China, indicating the strong oxidation capacity in

483 YRD region from the perspective of OH radical concentration. The modelled k_{OH} varied from 5 s^{-1} to 40 s^{-1}

484 over the whole campaign, and 40% of which could be explained by OVOCs, in which measured and

485 modelled OVOCs made up comparable contributions.

486 The radical primary source was dominated by HONO photolysis during this campaign, contributing 42% of

487 $P(RO_x)$. The secondary contributor was the photolysis of carbonyl compounds (including HCHO),

488 accounting for 24% of the total radical primary source. Radical termination was dominated by the reactions

489 with NO_x in the morning and peroxy radical self-reactions in the afternoon. Specifically, OH+NO_2 reaction

490 and peroxy radical self-reaction from HO_2+RO_2 were the most important pathways, contributing 25% and

491 33% of the total radical loss rates, respectively.

492 The comparison between observation and box model simulation showed generally good agreement for both

493 OH and HO_2 radicals on average. However, the OH radical showed a tendency of underestimation towards

494 low NO regime (NO< 0.1 ppb), and the discrepancy (42%) was beyond the measurement-model combined

495 uncertainty. The up-to-date H-shift mechanism of isoprene derived peroxy radicals could not explain the

496 discrepancy due to the low isoprene concentration (0.2 ppb) during this campaign. A genetic OH recycling

497 process equivalent to 100 ppt NO was capable to fill the gaps, which was also found in previous campaigns

498 in Backgarden, Yufa, Heshan, and Wangdu in China. In addition, the good simulation in HO_2 radical was

499 different from other monoterpene-rich forest environments, where HO_2 underestimations were found.

500 Additional sensitivity tests were performed to investigate the impact of monoterpenes and HO_2

501 heterogeneous uptake on radical chemistry in this study. Model simulation without monoterpene input or

502 allocating monoterpene to a different isomer (α-pinene and Limonene in this study) showed that HO_x radical

503 concentrations were not sensitive to the monoterpene in this study. In fact, the modelled RO_2 radical

504 concentration would be reduced by 23% without monoterpene constrained. The reduced RO_2 radical offset

505 the enhancement of HO_x radicals. The combined influence caused the net daily integrated ozone production

506 decreased by 6.3 ppb compared to the base model of 61.4 ppb, which demonstrated the importance of

507 monoterpene chemistry on the photochemical ozone production in this study. The role of HO_2 heterogeneous

508 uptake was tested by adding a pseudo first-order reaction loss of HO_2, and taking the effective uptake

509 coefficients of 0.2 and 0.08, respectively. The sensitivity test suggested the applied chemical mechanism

510   without HO_2 heterogeneous uptake could capture the key processes for HO_x radicals, and the effective uptake

511   coefficient should be less than 0.2, if the HO_2 heterogeneous loss played a role in this study, otherwise, the

512   HO_2 measurement-model discrepancy would be beyond the combined uncertainty. The daily integrated net

513   ozone production would reduce by 4.8 ppb, if the effective uptake coefficient was assumed to be 0.08.

514   Additionally, the noontime ozone production rate was 11.4 ppb h^{-1}, which was much slower than other

515   campaigns in urban and suburban areas varying from 13.9 to 65 ppb h^{-1}. Thus, the ozone production

516   efficiency calculated from the ratio of $P(O_x)$ and $P(RO_x)$ was only 1.7 in this study, which was comparable

517   to the values in rural campaigns but was 3 to 7 times lower than the values in other urban and suburban

518   campaigns, indicating the slow radical propagation rate and short chain length in this study.

519

522

523   *Author contributions.* YZ and KL organized the field campaign. KL and YZ designed the experiments.

524   XM and ZT analyzed the data. XM wrote the manuscript with input from ZT. All authors contributed to

525   measurements, discussing results, and commenting on the manuscript.

526

528

534   **References:**

535   Ding, A. J., Fu, C. B., Yang, X. Q., Sun, J. N., Zheng, L. F., Xie, Y. N., Herrmann, E., Nie, W., Petaja, T., Kerminen,

536   V. M., and Kulmala, M.: Ozone and fine particle in the western Yangtze River Delta: an overview of 1 yr

537   data at the SORPES station, Atmos. Chem. Phys., 13, 5813-5830, 10.5194/acp-13-5813-2013, 2013.

538   Dusanter, S., Vimal, D., Stevens, P. S., Volkamer, R., and Molina, L. T.: Measurements of OH and HO2

539   concentrations during the MCMA-2006 field campaign - Part 1: Deployment of the Indiana University laser-

540   induced fluorescence instrument, Atmos. Chem. Phys., 9, 1665-1685, 2009a.

541   Dusanter, S., Vimal, D., Stevens, P. S., Volkamer, R., Molina, L. T., Baker, A., Meinardi, S., Blake, D., Sheehy, P.,

542   Merten, A., Zhang, R., Zheng, J., Fortner, E. C., Junkermann, W., Dubey, M., Rahn, T., Eichinger, B.,

543   Lewandowski, P., Prueger, J., and Holder, H.: Measurements of OH and HO2 concentrations during the

544   MCMA-2006 field campaign - Part 2: Model comparison and radical budget, Atmospheric Chemistry and

545   Physics, 9, 6655-6675, 2009b.

546   Emmerson, K. M., Carslaw, N., Carslaw, D. C., Lee, J. D., McFiggans, G., Bloss, W. J., Gravestock, T., Heard, D.
547   E., Hopkins, J., Ingham, T., Pilling, M. J., Smith, S. C., Jacob, M., and Monks, P. S.: Free radical modelling
548   studies during the UK TORCH Campaign in Summer 2003, Atmospheric Chemistry and Physics, 7, 167-181,
549   2007.

550   Feiner, P. A., Brune, W. H., Miller, D. O., Zhang, L., Cohen, R. C., Romer, P. S., Goldstein, A. H., Keutsch, F. N.,
551   Skog, K. M., Wennberg, P. O., Nguyen, T. B., Teng, A. P., DeGouw, J., Koss, A., Wild, R. J., Brown, S. S.,
552   Guenther, A., Edgerton, E., Baumann, K., and Fry, J. L.: Testing Atmospheric Oxidation in an Alabama Forest,
553   Journal of the Atmospheric Sciences, 73, 4699-4710, 10.1175/jas-d-16-0044.1, 2016.

554   Fuchs, H., Tan, Z., Lu, K., Bohn, B., Broch, S., Brown, S. S., Dong, H., Gomm, S., Haeseler, R., He, L.,
555   Hofzumahaus, A., Holland, F., Li, X., Liu, Y., Lu, S., Min, K.-E., Rohrer, F., Shao, M., Wang, B., Wang, M.,
556   Wu, Y., Zeng, L., Zhang, Y., Wahner, A., and Zhang, Y.: OH reactivity at a rural site (Wangdu) in the North
557   China Plain: contributions from OH reactants and experimental OH budget, Atmospheric Chemistry and
558   Physics, 17, 645-661, 10.5194/acp-17-645-2017, 2017.

559   Geng, F., Mao, X., Zhou, M., Zhong, S., and Lenschow, D.: Multi-year ozone concentration and its spectra in
560   Shanghai, China, Science of the Total Environment, 521-522, 135-143,
561   https://doi.org/10.1016/j.scitotenv.2015.03.082, 2015.

562   George, I. J., Matthews, P. S. J., Whalley, L. K., Brooks, B., Goddard, A., Baeza-Romero, M. T., and Heard, D.
563   E.: Measurements of uptake coefficients for heterogeneous loss of HO2 onto submicron inorganic salt
564   aerosols, Physical Chemistry Chemical Physics, 15, 12829-12845, https://doi.org/10.1039/C3CP51831K,
565   2013.

566   Goliff, W. S., Stockwell, W. R., and Lawson, C. V.: The regional atmospheric chemistry mechanism, version 2,
567   Atmospheric Environment, 68, 174-185, https://doi.org/10.1016/j.atmosenv.2012.11.038, 2013.

568   Griffith, S. M., Hansen, R. F., Dusanter, S., Michoud, V., Gilman, J. B., Kuster, W. C., Veres, P. R., Graus, M., de
569   Gouw, J. A., Roberts, J., Young, C., Washenfelder, R., Brown, S. S., Thalman, R., Waxman, E., Volkamer, R.,
570   Tsai, C., Stutz, J., Flynn, J. H., Grossberg, N., Lefer, B., Alvarez, S. L., Rappenglueck, B., Mielke, L. H.,
571   Osthoff, H. D., and Stevens, P. S.: Measurements of hydroxyl and hydroperoxy radicals during CalNex-LA:
572   Model comparisons and radical budgets, J. Geophys. Res.-Atmos., 121, 4211-4232, 10.1002/2015jd024358,
573   2016.

574   Hens, K., Novelli, A., Martinez, M., Auld, J., Axinte, R., Bohn, B., Fischer, H., Keronen, P., Kubistin, D., Nölscher,
575   A. C., Oswald, R., Paasonen, P., Petäjä, T., Regelin, E., Sander, R., Sinha, V., Sipilä, M., Taraborrelli, D.,
576   Tatum Ernest, C., Williams, J., Lelieveld, J., and Harder, H.: Observation and modelling of HOx radicals in
577   a boreal forest, Atmos. Chem. Phys., 14, 8723-8747, https://doi.org/10.5194/acp-14-8723-2014, 2014.

578   Hofzumahaus, A., Aschmutat, U., Hessling, M., Holland, F., and Ehhalt, D. H.: The measurement of tropospheric
579   OH radicals by laser-induced fluorescence spectroscopy during the POPCORN field campaign, Geophys.
580   Res. Lett., 23, 2541-2544, https://doi.org/10.1029/96gl02205, 1996.

581   Hofzumahaus, A., Aschmutat, U., Brandenburger, U., Brauers, T., Dorn, H. P., Hausmann, M., Hessling, M.,
582   Holland, F., Plass-Dulmer, C., and Ehhalt, D. H.: Intercomparison of tropospheric OH measurements by
583   different laser techniques during the POPCORN campaign 1994, Journal of Atmospheric Chemistry, 31, 227-
584   246, 10.1023/a:1006014707617, 1998.

585   Hofzumahaus, A., Rohrer, F., Lu, K., Bohn, B., Brauers, T., Chang, C.-C., Fuchs, H., Holland, F., Kita, K., Kondo,
586   Y., Li, X., Lou, S., Shao, M., Zeng, L., Wahner, A., and Zhang, Y.: Amplified Trace Gas Removal in the

587   Troposphere, Science, 324, 1702-1704, https://doi.org/10.1126/science.1164566, 2009.

588 Holland, F., Aschmutat, U., Hessling, M., Hofzumahaus, A., and Ehhalt, D. H.: Highly time resolved
589   measurements of OH during POPCORN using laser-induced fluorescence spectroscopy, J. Atmos. Sci., 31,
590   205-225, https://doi.org/10.1023/a:1005868520002, 1998.

591 Holland, F., Hofzumahaus, A., Schäfer, J., Kraus, A., and Pätz, H. W.: Measurements of OH and HO2 radical
592   concentrations and photolysis frequencies during BERLIOZ, J. Geophys. Res., 108,
593   https://doi.org/10.1029/2001JD001393, 2003.

594 Kanaya, Y., Cao, R., Akimoto, H., Fukuda, M., Komazaki, Y., Yokouchi, Y., Koike, M., Tanimoto, H., Takegawa,
595   N., and Kondo, Y.: Urban photochemistry in central Tokyo: 1. Observed and modeled OH and HO2radical
596   concentrations during the winter and summer of 2004, Journal of Geophysical Research, 112,
597   10.1029/2007jd008670, 2007.

598 Kanaya, Y., Fukuda, M., Akimoto, H., Takegawa, N., Komazaki, Y., Yokouchi, Y., Koike, M., and Kondo, Y.:
599   Urban photochemistry in central Tokyo: 2. Rates and regimes of oxidant (O3+ NO2) production, Journal of
600   Geophysical Research, 113, 10.1029/2007jd008671, 2008.

601 Kim, S., Wolfe, G. M., Mauldin, L., Cantrell, C., Guenther, A., Karl, T., Turnipseed, A., Greenberg, J., Hall, S. R.,
602   Ullmann, K., Apel, E., Hornbrook, R., Kajii, Y., Nakashima, Y., Keutsch, F. N., DiGangi, J. P., Henry, S. B.,
603   Kaser, L., Schnitzhofer, R., Graus, M., Hansel, A., Zheng, W., and Flocke, F. F.: Evaluation of HOx sources
604   and cycling using measurement-constrained model calculations in a 2-methyl-3-butene-2-ol (MBO) and
605   monoterpene (MT) dominated ecosystem, Atmos. Chem. Phys., 13, 2031-2044, 10.5194/acp-13-2031-2013,
606   2013.

607 Lakey, P. S. J., George, I. J., Whalley, L. K., Baeza-Romero, M. T., and Heard, D. E.: Measurements of the HO2
608   Uptake Coefficients onto Single Component Organic Aerosols, Environmental Science & Technology, 49,
609   4878-4885, https://doi.org/10.1021/acs.est.5b00948, 2015.

610 Lee, B. H., Wood, E. C., Herndon, S. C., Lefer, B. L., Luke, W. T., Brune, W. H., Nelson, D. D., Zahniser, M. S.,
611   and Munger, J. W.: Urban measurements of atmospheric nitrous acid: A caveat on the interpretation of the
612   HONO photostationary state, J. Geophys. Res.-Atmos., 118, 12274-12281, 10.1002/2013jd020341, 2013.

613 Lelieveld, J., Butler, T. M., Crowley, J. N., Dillon, T. J., Fischer, H., Ganzeveld, L., Harder, H., Lawrence, M. G.,
614   Martinez, M., Taraborrelli, D., and Williams, J.: Atmospheric oxidation capacity sustained by a tropical forest,
615   Nature, 452, 737-740, https://doi.org/10.1038/nature06870, 2008.

616 Li, K., Jacob, D. J., Liao, H., Shen, L., Zhang, Q., and Bates, K. H.: Anthropogenic drivers of 2013-2017 trends
617   in summer surface ozone in China, Proceedings of the National Academy of Sciences of the United States of
618   America, 116, 422-427, https://doi.org/10.1073/pnas.1812168116, 2019.

619 Liu, Y., Zhao, Q., Hao, X., Zhao, J., Zhang, Y., Yang, X., Fu, Q., Xu, X., Wang, X., Huo, J., and Chen, J.: Increasing
620   surface ozone and enhanced secondary organic carbon formation at a city junction site: An epitome of the
621   Yangtze River Delta, China (2014–2017), Environmental Pollution, 265, 114847,
622   https://doi.org/10.1016/j.envpol.2020.114847, 2020.

623 Lou, S., Holland, F., Rohrer, F., Lu, K., Bohn, B., Brauers, T., Chang, C. C., Fuchs, H., Haeseler, R., Kita, K.,
624   Kondo, Y., Li, X., Shao, M., Zeng, L., Wahner, A., Zhang, Y., Wang, W., and Hofzumahaus, A.: Atmospheric
625   OH reactivities in the Pearl River Delta - China in summer 2006: measurement and model results,
626   Atmospheric Chemistry and Physics, 10, 11243-11260, 10.5194/acp-10-11243-2010, 2010.

627 Lu, K., Guo, S., Tan, Z., Wang, H., Shang, D., Liu, Y., Li, X., Wu, Z., Hu, M., and Zhang, Y.: Exploring
628   atmospheric free-radical chemistry in China: the self-cleansing capacity and the formation of secondary air

629   pollution, Natl Sci Rev, 6, 579-594, 10.1093/nsr/nwy073, 2019.

630   Lu, K. D., Rohrer, F., Holland, F., Fuchs, H., Bohn, B., Brauers, T., Chang, C. C., Häseler, R., Hu, M., Kita, K.,
631   Kondo, Y., Li, X., Lou, S. R., Nehr, S., Shao, M., Zeng, L. M., Wahner, A., Zhang, Y. H., and Hofzumahaus,
632   A.: Observation and modelling of OH and HO_2 concentrations in the Pearl River Delta 2006: a
633   missing OH source in a VOC rich atmosphere, Atmospheric Chemistry and Physics, 12, 1541-1569,
634   10.5194/acp-12-1541-2012, 2012.

635   Lu, K. D., Hofzumahaus, A., Holland, F., Bohn, B., Brauers, T., Fuchs, H., Hu, M., Häseler, R., Kita, K., Kondo,
636   Y., Li, X., Lou, S. R., Oebel, A., Shao, M., Zeng, L. M., Wahner, A., Zhu, T., Zhang, Y. H., and Rohrer, F.:
637   Missing OH source in a suburban environment near Beijing: observed and modelled OH and
638   HO_2 concentrations in summer 2006, Atmospheric Chemistry and Physics, 13, 1057-1080,
639   10.5194/acp-13-1057-2013, 2013.

640   Lu, X., Hong, J., Zhang, L., Cooper, O. R., Schultz, M. G., Xu, X., Wang, T., Gao, M., Zhao, Y., and Zhang, Y.:
641   Severe Surface Ozone Pollution in China: A Global Perspective, Environ. Sci. Technol. Lett., 5, 487-494,
642   10.1021/acs.estlett.8b00366, 2018.

643   Ma, X., Tan, Z., Lu, K., Yang, X., Liu, Y., Li, S., Li, X., Chen, S., Novelli, A., Cho, C., Zeng, L., Wahner, A., and
644   Zhang, Y.: Winter photochemistry in Beijing: Observation and model simulation of OH and HO2 radicals at
645   an urban site, Science of The Total Environment, 685, 85-95, https://doi.org/10.1016/j.scitotenv.2019.05.329,
646   2019.

647   Mao, J., Ren, X., Chen, S., Brune, W. H., Chen, Z., Martinez, M., Harder, H., Lefer, B., Rappenglück, B., Flynn,
648   J., and Leuchner, M.: Atmospheric oxidation capacity in the summer of Houston 2006: Comparison with
649   summer measurements in other metropolitan studies, Atmospheric Environment, 44, 4107-4115,
650   10.1016/j.atmosenv.2009.01.013, 2010.

651   Mao, J., Ren, X., Zhang, L., Van Duin, D. M., Cohen, R. C., Park, J. H., Goldstein, A. H., Paulot, F., Beaver, M.
652   R., Crounse, J. D., Wennberg, P. O., DiGangi, J. P., Henry, S. B., Keutsch, F. N., Park, C., Schade, G. W.,
653   Wolfe, G. M., Thornton, J. A., and Brune, W. H.: Insights into hydroxyl measurements and atmospheric
654   oxidation in a California forest, Atmospheric Chemistry and Physics, 12, 8009-8020, 10.5194/acp-12-8009-
655   2012, 2012.

656   Martinez, M.: OH and HO2concentrations, sources, and loss rates during the Southern Oxidants Study in
657   Nashville, Tennessee, summer 1999, Journal of Geophysical Research, 108, 10.1029/2003jd003551, 2003.

658   Michoud, V., Kukui, A., Camredon, M., Colomb, A., Borbon, A., Miet, K., Aumont, B., Beekmann, M., Durand-
659   Jolibois, R., Perrier, S., Zapf, P., Siour, G., Ait-Helal, W., Locoge, N., Sauvage, S., Afif, C., Gros, V., Furger,
660   M., Ancellet, G., and Doussin, J. F.: Radical budget analysis in a suburban European site during the
661   MEGAPOLI summer field campaign, Atmospheric Chemistry and Physics, 12, 11951-11974, 10.5194/acp-
662   12-11951-2012, 2012.

663   Molina, L. T., Madronich, S., Gaffney, J. S., Apel, E., de Foy, B., Fast, J., Ferrare, R., Herndon, S., Jimenez, J. L.,
664   Lamb, B., Osornio-Vargas, A. R., Russell, P., Schauer, J. J., Stevens, P. S., Volkamer, R., and Zavala, M.: An
665   overview of the MILAGRO 2006 Campaign: Mexico City emissions and their transport and transformation,
666   Atmos. Chem. Phys., 10, 8697-8760, 10.5194/acp-10-8697-2010, 2010.

667   Novelli, A., Hens, K., Ernest, C. T., Kubistin, D., Regelin, E., Elste, T., Plass-Duelmer, C., Martinez, M., Lelieveld,
668   J., and Harder, H.: Characterisation of an inlet pre-injector laser-induced fluorescence instrument for the
669   measurement of atmospheric hydroxyl radicals, Atmospheric Measurement Techniques, 7, 3413-3430,
670   10.5194/amt-7-3413-2014, 2014.

671   Novelli, A., Hens, K., Ernest, C. T., Martinez, M., Noelscher, A. C., Sinha, V., Paasonen, P., Petaja, T., Sipila, M.,
672   Elste, T., Plass-Duelmer, C., Phillips, G. J., Kubistin, D., Williams, J., Vereecken, L., Lelieveld, J., and Harder,
673   H.: Estimating the atmospheric concentration of Criegee intermediates and their possible interference in a
674   FAGE-LIF instrument, Atmospheric Chemistry and Physics, 17, 7807-7826, 10.5194/acp-17-7807-2017,
675   2017.
676   Peeters, J., Nguyen, T. L., and Vereecken, L.: HOx radical regeneration in the oxidation of isoprene, Physical
677   Chemistry Chemical Physics, 11, 5935-5939, 10.1039/b908511d, 2009.
678   Peeters, J., Muller, J.-F., Stavrakou, T., and Nguyen, V. S.: Hydroxyl radical recycling in isoprene oxidation driven
679   by hydrogen bonding and hydrogen tunneling: The upgraded LIM1 mechanism, The Journal of Physical
680   Chemistry A, 118, 8625-8643, https://doi.org/10.1021/jp5033146, 2014.
681   Platt, U., Alicke, B., Dubois, R., Geyer, A., Hofzumahaus, A., Holland, F., Martinez, M., Mihelcic, D., Klupfel,
682   T., Lohrmann, B., Patz, W., Perner, D., Rohrer, F., Schafer, J., and Stutz, J.: Free radicals and fast
683   photochemistry   during   BERLIOZ,   Journal   of   Atmospheric   Chemistry,   42,   359-394,
684   10.1023/a:1015707531660, 2002.
685   Ren, X., Olson, J. R., Crawford, J. H., Brune, W. H., Mao, J., Long, R. B., Chen, Z., Chen, G., Avery, M. A.,
686   Sachse, G. W., Barrick, J. D., Diskin, G. S., Huey, L. G., Fried, A., Cohen, R. C., Heikes, B., Wennberg, P.
687   O., Singh, H. B., Blake, D. R., and Shetter, R. E.: HOx chemistry during INTEX-A 2004: Observation, model
688   calculation,   and   comparison   with   previous   studies,   J.   Geophys.   Res.,   113,   310,
689   https://doi.org/10.1029/2007JD009166, 2008.
690   Ren, X., van Duin, D., Cazorla, M., Chen, S., Mao, J., Zhang, L., Brune, W. H., Flynn, J. H., Grossberg, N., Lefer,
691   B. L., Rappenglück, B., Wong, K. W., Tsai, C., Stutz, J., Dibb, J. E., Thomas Jobson, B., Luke, W. T., and
692   Kelley, P.: Atmospheric oxidation chemistry and ozone production: Results from SHARP 2009 in Houston,
693   Texas, Journal of Geophysical Research: Atmospheres, 118, 5770-5780, 10.1002/jgrd.50342, 2013.
694   Ren, X. R., Harder, H., Martinez, M., Lesher, R. L., Oliger, A., Shirley, T., Adams, J., Simpas, J. B., and Brune,
695   W. H.: HOx concentrations and OH reactivity observations in New York City during PMTACS-NY2001,
696   Atmospheric Environment, 37, 3627-3637, 10.1016/s1352-2310(03)00460-6, 2003a.
697   Ren, X. R., Harder, H., Martinez, M., Lesher, R. L., Oliger, A., Simpas, J. B., Brune, W. H., Schwab, J. J.,
698   Demerjian, K. L., He, Y., Zhou, X. L., and Gao, H. G.: OH and HO2 chemistry in the urban atmosphere of
699   New York City, Atmospheric Environment, 37, 3639-3651, 10.1016/s1352-2310(03)00459-x, 2003b.
700   Rickly, P., and Stevens, P. S.: Measurements of a potential interference with laser-induced fluorescence
701   measurements of ambient OH from the ozonolysis of biogenic alkenes, Atmos. Meas. Tech., 11, 1-16,
702   10.5194/amt-11-1-2018, 2018.
703   Rohrer, F., Lu, K., Hofzumahaus, A., Bohn, B., Brauers, T., Chang, C.-C., Fuchs, H., Haeseler, R., Holland, F.,
704   Hu, M., Kita, K., Kondo, Y., Li, X., Lou, S., Oebel, A., Shao, M., Zeng, L., Zhu, T., Zhang, Y., and Wahner,
705   A.: Maximum efficiency in the hydroxyl-radical-based self-cleansing of the troposphere, Nature Geoscience,
706   7, 559-563, 10.1038/ngeo2199, 2014.
707   Shirley, T. R., Brune, W. H., Ren, X., Mao, J., Lesher, R., Cardenas, B., Volkamer, R., Molina, L. T., Molina, M.
708   J., Lamb, B., Velasco, E., Jobson, T., and Alexander, M.: Atmospheric oxidation in the Mexico City
709   Metropolitan Area (MCMA) during April 2003, Atmospheric Chemistry and Physics, 6, 2753-2765, 2006.
710   Stone, D., Evans, M. J., Edwards, P. M., Commane, R., Ingham, T., Rickard, A. R., Brookes, D. M., Hopkins, J.,
711   Leigh, R. J., Lewis, A. C., Monks, P. S., Oram, D., Reeves, C. E., Stewart, D., and Heard, D. E.: Isoprene
712   oxidation mechanisms: measurements and modelling of OH and HO2 over a South-East Asian tropical

713   rainforest during the OP3 field campaign, Atmos. Chem. Phys., 11, 6749-6771, 10.5194/acp-11-6749-2011,
714   2011.
715   Stone, D., Whalley, L. K., and Heard, D. E.: Tropospheric OH and HO2 radicals: field measurements and model
716   comparisons, Chemical Society Reviews, 41, 6348-6404, 10.1039/c2cs35140d, 2012.
717   Taketani, F., Kanaya, Y., and Akimoto, H.: Heterogeneous loss of HO2 by KCl, synthetic sea salt, and natural
718   seawater   aerosol   particles,   Atmospheric   Environment,   43,   1660-1665,
719   https://doi.org/10.1016/j.atmosenv.2008.12.010, 2009.
720   Taketani, F., and Kanaya, Y.: Kinetics of HO2 Uptake in Levoglucosan and Polystyrene Latex Particles, The
721   Journal of Physical Chemistry Letters, 1, 1701-1704, https://doi.org/10.1021/jz100478s, 2010.
722   Taketani, F., Kanaya, Y., Pochanart, P., Liu, Y., Li, J., Okuzawa, K., Kawamura, K., Wang, Z., and Akimoto, H.:
723   Measurement of overall uptake coefficients for HO2 radicals by aerosol particles sampled from ambient air
724   at Mts. Tai and Mang (China), Atmos. Chem. Phys., 12, 11907-11916, https://doi.org/10.5194/acp-12-11907-
725   2012, 2012.
726   Tan, D., Faloona, I., Simpas, J. B., Brune, W., Shepson, P. B., Couch, T. L., Sumner, A. L., Carroll, M. A.,
727   Thornberry, T., Apel, E., Riemer, D., and Stockwell, W.: HOx budgets in a deciduous forest: Results from
728   the   PROPHET   summer   1998   campaign,   J.   Geophys.   Res.,   106,   24407-24427,
729   https://doi.org/10.1029/2001jd900016, 2001.
730   Tan, Z., Fuchs, H., Lu, K., Hofzumahaus, A., Bohn, B., Broch, S., Dong, H., Gomm, S., Haeseler, R., He, L.,
731   Holland, F., Li, X., Liu, Y., Lu, S., Rohrer, F., Shao, M., Wang, B., Wang, M., Wu, Y., Zeng, L., Zhang, Y.,
732   Wahner, A., and Zhang, Y.: Radical chemistry at a rural site (Wangdu) in the North China Plain: observation
733   and model calculations of OH, HO2 and RO2 radicals, Atmospheric Chemistry and Physics, 17, 663-690,
734   10.5194/acp-17-663-2017, 2017.
735   Tan, Z., Lu, K., Dong, H., Hu, M., Li, X., Liu, Y., Lu, S., Shao, M., Su, R., Wang, H., Wu, Y., Wahner, A., and
736   Zhang, Y.: Explicit diagnosis of the local ozone production rate and the ozone-NOx-VOC sensitivities, Sci
737   Bull, 63, 1067-1076, 10.1016/j.scib.2018.07.001, 2018a.
738   Tan, Z., Lu, K., Jiang, M., Su, R., Dong, H., Zeng, L., Xie, S., Tan, Q., and Zhang, Y.: Exploring ozone pollution
739   in Chengdu, southwestern China: A case study from radical chemistry to O-3-VOC-NOx sensitivity, Science
740   of the Total Environment, 636, 775-786, 10.1016/j.scitotenv.2018.04.286, 2018b.
741   Tan, Z., Rohrer, F., Lu, K., Ma, X., Bohn, B., Broch, S., Dong, H., Fuchs, H., Gkatzelis, G. I., Hofzumahaus, A.,
742   Holland, F., Li, X., Liu, Y., Liu, Y., Novelli, A., Shao, M., Wang, H., Wu, Y., Zeng, L., Hu, M., Kiendler-
743   Scharr, A., Wahner, A., and Zhang, Y.: Wintertime photochemistry in Beijing: observations of ROx radical
744   concentrations in the North China Plain during the BEST-ONE campaign, Atmospheric Chemistry and
745   Physics, 18, 12391-12411, 10.5194/acp-18-12391-2018, 2018c.
746   Tan, Z., Lu, K., Hofzumahaus, A., Fuchs, H., Bohn, B., Holland, F., Liu, Y., Rohrer, F., Shao, M., Sun, K., Wu, Y.,
747   Zeng, L., Zhang, Y., Zou, Q., Kiendler-Scharr, A., Wahner, A., and Zhang, Y.: Experimental budgets of OH,
748   HO2, and RO2 radicals and implications for ozone formation in the Pearl River Delta in China 2014, Atmos.
749   Chem. Phys., 19, 7129-7150, https://doi.org/10.5194/acp-19-7129-2019, 2019a.
750   Tan, Z., Lu, K., Jiang, M., Su, R., Wang, H., Lou, S., Fu, Q., Zhai, C., Tan, Q., Yue, D., Chen, D., Wang, Z., Xie,
751   S., Zeng, L., and Zhang, Y.: Daytime atmospheric oxidation capacity in four Chinese megacities during the
752   photochemically polluted season: a case study based on box model simulation, Atmos. Chem. Phys., 19,
753   3493-3513, https://doi.org/10.5194/acp-19-3493-2019, 2019b.
754   Tan, Z., Hofzumahaus, A., Lu, K., Brown, S. S., Holland, F., Huey, L. G., Kiendler-Scharr, A., Li, X., Liu, X., Ma,

755   N., Min, K.-E., Rohrer, F., Shao, M., Wahner, A., Wang, Y., Wiedensohler, A., Wu, Y., Wu, Z., Zeng, L.,
756   Zhang, Y., and Fuchs, H.: No Evidence for a Significant Impact of Heterogeneous Chemistry on Radical
757   Concentrations in the North China Plain in Summer 2014, Environmental Science & Technology,
758   10.1021/acs.est.0c00525, 2020.

759   Thornton, J. A., Wooldridge, P. J., Cohen, R. C., Martinez, M., Harder, H., Brune, W. H., Williams, E. J., Roberts,
760   J. M., Fehsenfeld, F. C., Hall, S. R., Shetter, R. E., Wert, B. P., and Fried, A.: Ozone production rates as a
761   function of NOx abundances and HOx production rates in the Nashville urban plume, Journal of Geophysical
762   Research-Atmospheres, 107, 10.1029/2001jd000932, 2002.

763   Thornton, J. A., Jaegle, L., and McNeill, V. F.: Assessing known pathways for HO2 loss in aqueous atmospheric
764   aerosols: Regional and global impacts on tropospheric oxidants, Journal of Geophysical Research:
765   Atmospheres, 113, https://doi.org/10.1029/2007jd009236, 2008.

766   Tie, X., Geng, F., Guenther, A., Cao, J., Greenberg, J., Zhang, R., Apel, E., Li, G., Weinheimer, A., Chen, J., and
767   Cai, C.: Megacity impacts on regional ozone formation: observations and WRF-Chem modeling for the
768   MIRAGE-Shanghai field campaign, Atmos. Chem. Phys., 13, 5655-5669, https://doi.org/10.5194/acp-13-
769   5655-2013, 2013.

770   Volz-Thomas, A., Patz, H. W., Houben, N., Konrad, S., Mihelcic, D., Klupfel, T., and Perner, D.: Inorganic trace
771   gases and peroxy radicals during BERLIOZ at Pabstthum: An investigation of the photostationary state of
772   NOx and O-3, Journal of Geophysical Research-Atmospheres, 108, 10.1029/2001jd001255, 2003.

773   Wang, F. Y., Hu, R. Z., Chen, H., Xie, P. H., Wang, Y. H., Li, Z. Y., Jin, H. W., Liu, J. G., and Liu, W. Q.:
774   Development of a field system for measurement of tropospheric OH radical using laser-induced fluorescence
775   technique, Opt Express, 27, A419-A435, 10.1364/Oe.27.00a419, 2019a.

776   Wang, H., Chen, X., Lu, K., Hu, R., Li, Z., Wang, H., Ma, X., Yang, X., Chen, S., Dong, H., Liu, Y., Fang, X.,
777   Zeng, L., Hu, M., and Zhang, Y.: NO3 and N2O5 chemistry at a suburban site during the EXPLORE-YRD
778   campaign in 2018, Atmospheric Environment, 224, 117180, https://doi.org/10.1016/j.atmosenv.2019.117180,
779   2020a.

780   Wang, Y., Li, W., Gao, W., Liu, Z., Tian, S., Shen, R., Ji, D., Wang, S., Wang, L., Tang, G., Song, T., Cheng, M.,
781   Wang, G., Gong, Z., Hao, J., and Zhang, Y.: Trends in particulate matter and its chemical compositions in
782   China from 2013–2017, Science China Earth Sciences, 10.1007/s11430-018-9373-1, 2019b.

783   Wang, Y., Gao, W., Wang, S., Song, T., Gong, Z., Ji, D., Wang, L., Liu, Z., Tang, G., Huo, Y., Tian, S., Li, J., Li,
784   M., Yang, Y., Chu, B., Petäjä, T., Kerminen, V.-M., He, H., Hao, J., Kulmala, M., Wang, Y., and Zhang, Y.:
785   Contrasting trends of PM2.5 and surface-ozone concentrations in China from 2013 to 2017, Natl Sci Rev,
786   10.1093/nsr/nwaa032, 2020b.

787   Whalley, L. K., Edwards, P. M., Furneaux, K. L., Goddard, A., Ingham, T., Evans, M. J., Stone, D., Hopkins, J.
788   R., Jones, C. E., Karunaharan, A., Lee, J. D., Lewis, A. C., Monks, P. S., Moller, S. J., and Heard, D. E.:
789   Quantifying the magnitude of a missing hydroxyl radical source in a tropical rainforest, Atmos. Chem. Phys.,
790   11, 7223-7233, https://doi.org/10.5194/acp-11-7223-2011, 2011.

791   Whalley, L. K.: Atmospheric OH reactivity in central London: observations, model predictions and estimates of
792   in situ ozone production, Atmospheric Chemistry and Physics, - 16, - 2122, 2016.

793   Whalley, L. K., Stone, D., Dunmore, R., Hamilton, J., Hopkins, J. R., Lee, J. D., Lewis, A. C., Williams, P.,
794   Kleffmann, J., Laufs, S., Woodward-Massey, R., and Heard, D. E.: Understanding in situ ozone production
795   in the summertime through radical observations and modelling studies during the Clean air for London
796   project (ClearfLo), Atmospheric Chemistry and Physics, 18, 2547-2571, 10.5194/acp-18-2547-2018, 2018.

797   Wolfe, G. M., Cantrell, C., Kim, S., Mauldin Iii, R. L., Karl, T., Harley, P., Turnipseed, A., Zheng, W., Flocke, F.,
798   Apel, E. C., Hornbrook, R. S., Hall, S. R., Ullmann, K., Henry, S. B., DiGangi, J. P., Boyle, E. S., Kaser, L.,
799   Schnitzhofer, R., Hansel, A., Graus, M., Nakashima, Y., Kajii, Y., Guenther, A., and Keutsch, F. N.: Missing
800   peroxy radical sources within a summertime ponderosa pine forest, Atmos. Chem. Phys., 14, 4715-4732,
801   10.5194/acp-14-4715-2014, 2014.
802   Xing, C., Liu, C., Wang, S., Chan, K. L., Gao, Y., Huang, X., Su, W., Zhang, C., Dong, Y., Fan, G., Zhang, T.,
803   Chen, Z., Hu, Q., Su, H., Xie, Z., and Liu, J.: Observations of the vertical distributions of summertime
804   atmospheric pollutants and the corresponding ozone production in Shanghai, China, Atmos. Chem. Phys., 17,
805   14275-14289, 10.5194/acp-17-14275-2017, 2017.
806   Yang, X., Wang, H., Tan, Z., Lu, K., and Zhang, Y.: Observations of OH Radical Reactivity in Field Studies, Acta
807   Chimica Sinica, 77, 613-624, 10.6023/a19030094, 2019.
808   Yang, Y., Shao, M., Wang, X., Noelscher, A. C., Kessel, S., Guenther, A., and Williams, J.: Towards a quantitative
809   understanding of total OH reactivity: A review, Atmospheric Environment, 134, 147-161,
810   10.1016/j.atmosenv.2016.03.010, 2016.
811   Zhang, K., Xu, J. L., Huang, Q., Zhou, L., Fu, Q. Y., Duan, Y. S., and Xiu, G. L.: Precursors and potential sources
812   of ground-level ozone in suburban Shanghai, Front Env Sci Eng, 14, ARTN 92
813   10.1007/s11783-020-1271-8, 2020.
814   Zou, Q., Song, H., Tang, M. J., and Lu, K. D.: Measurements of HO2 uptake coefficient on aqueous (NH4)(2)SO4
815   aerosol using aerosol flow tube with LIF system, Chinese Chem Lett, 30, 2236-2240,
816   10.1016/j.cclet.2019.07.041, 2019.
817
818

819 **Table 1 Measured species and performance of the instruments.**

Parameters	Techniques	Time resolutions	Limit of Detection[a]	Accuracy
OH	LIF[b]	30 s	6.0×10^5 cm^{-3}	±10%
HO$_2$	LIF[b,c]	30 s	1.0×10^7 cm^{-3}	±13%
Photolysis frequencies	Spectroradiometer	9 s	[d]	±10%
O$_3$	UV photometry	60 s	0.5 ppb	±5%
NO	Chemiluminescence	60 s	60 ppt	±20%
NO$_2$	Chemiluminescence[e]	60 s	0.3 ppb	±20%
HONO	LOPAP[f]	60 s	10 ppt	±20%
CO	Infrared absorption	60 s	1 ppb	±1 ppb
SO$_2$	Pulsed UV fluorescence	60 s	0.1 ppb	±5%
VOCs[g]	GC-FID/MS[h]	1 h	20-300 ppt	±15%
HCHO	Hantzsch fluorimetry	60 s	25 ppt	±5%
Glyoxal	CEAS	60 s	60 ppt	±10%
Monoterpene[i]	PTR-MS	10 s	20 ppt	±15%
PNSD	SMPS	5 min	14 nm-700 nm	±20%

820   [a] Signal-to-noise ratio =1. [b] Laser Induced Fluorescence. [c] Chemical conversion to OH via NO reaction before detection. [d]

821   Process-specific, 5 orders of magnitude lower than maximum at noon. [e] Photolytic conversion to NO before detection, home-

822   built converter. [f] Long-path absorption photometry. [g] VOCs including C$_2$-C$_{11}$ alkanes, C$_2$-C$_6$ alkenes, C$_6$-C$_{10}$ aromatics. [h] Gas

823   chromatography equipped with a mass spectrometer and a flame ionization detector. [i] the sum of monoterpene.

824

825

826

827 **Table 2 Assignment of measured and constrained VOCs in RAMC2 during this study.**

RACM	Measured hydrocarbons
ACE	acetylene
ETH	ethane
HC3	propane, *i*-butane, *n*-butane, 2,2-dimethylbutane
HC5	*i*-pentane, *n*-pentane, cyclopentane, 2,3-dimethylbutane, 2-methylpentane, 3-methylpentane, MTBE, *n*-hexane, 2,3-dimethylpentane, 2,4-dimethylpentane, methylcyclopentane, 2-methylhexane
HC8	cyclohexane, 3-methylhexane, 2,2,4-trimethylpentane, 2,3,4-trimethylpentane, *n*-heptane, methylcyclohexane, 2-methylheptane, 3-methylheptane, *n*-octane, *n*-nonane, *n*-decane, *n*-undecane
ETE	ethylene
OLI	*trans*-2-butene, *cis*-2-butene, *trans*-2-pentene, *cis*-2-pentene
OLT	propene, 1-butene, 1-pentene, 1-hexene, styrene
DIEN	1,3-butadiene
BEN	benzene
TOL	toluene, ethylbenzene, *i*-propylbenzene, *n*-propylbenzene
XYO	*o*-xylene, *o*-ethyltoluene
XYM	*m*-ethyltoluene, 1,3,5-trimethylbenzene, 1,2,4-trimethylbenzene, 1,2,3-trimethylbenzene, *m*-diethylbenzene
XYP	*m,p*-xylene, *p*-ethyltoluene, *p*-diethylbenzene
ISO	isoprene
API	sum of monoterpenes
HCHO	formaldehyde
ACD	acetaldehyde
GLY	glyoxal
ACT	acetone
MACR	methacrolein
MVK	methyl vinyl ketone
MEK	methyl ethyl ketone

828

829

830

Atmospheric
Chemistry
and Physics
Discussions

Open Access

EGU

831

832

Table 3 Summary of filed measurements and model simulation for $j(O^1D)$, O_3, NO_x, OH, HO_2, $P(RO_x)$, $F(O_x)$ and OPE at local noon in urban and suburban environments.

Location	Month Year	Type	$j(O^1D)$ /10^{-5} s^{-1}	O_3 /ppb	NO_x /ppb	OH /10^6 cm^{-3}	HO_2 /10^8 cm^{-3}	$P(RO_x)$ /ppb/h	$F(O_x)$ /ppb/h	OPE[s]	References
Pabstthum, Germany, 52.85°N, 12.94°W, 50 km NW of Berlin	July-August 1998	Rural	1.5	42	1.55	3.5	2.2	1.7[a]	2.2[b]	1.3	(Holland et al., 2003;Volz-Thomas et al., 2003;Platt et al., 2002)
Nashville, USA, 36°11.4'N, 86°42.0'W, 8 km NE of downtown area	June-July 1999	Suburban	3.0[a]	60[a]	4.4[a]	10	7.5	1.1	9[c]	8.2	(Martinez, 2003;Thornton et al., 2002)
La Porte, USA, 29°40'N, 95°01'W, 40 km SE of Houston	August-September 2000	Suburban	3.0	70	6	20	7.5	4.9	25[d]	5.1	(Mao et al., 2010)
New York (Queens College), USA, 40°44'15''N, 73°49'18''W, in the Borough of Queens	June-August 2001	Urban	2.5	48	28	7.0[e]	1.0[e]	4.8	34[d]	7.1	(Mao et al., 2010;Ren et al., 2003b;Ren et al., 2003a)
Mexico City, Mexico, 19°25'N, ~7 km SE of downtown area	April-May 2003	Urban	4.5	115	18	12[f]	15[f]	8.6	65[d]	7.6	(Mao et al., 2010;Shirley et al., 2006)
Essex (Writtle College), England, 51°44'12''N, 0°25'28''E, 25 miles NE of central London	July-August 2003	Rural	1.0[g]	46.5[g]	10.8[g]	2[g]	0.7[g]	11.6[g]	7.2[g,h]	0.6	(Emmerson et al., 2007)

Atmospheric
Chemistry
and Physics
Discussions

Open Access

Site	Period	Type									Reference
Tokyo (University of Tokyo), Japan, 35°39'N, 139°41'E, near the city center	July-August 2004	Urban	2.5	32	12	6.3^e	1.4^e	2.2 (6.8)^i	13.9^i	6.3 (2.0)^i	(Kanaya et al., 2007;Kanaya et al., 2008)
Backgardon, China, 23.487°N, 113.034°E, 60 km NW of downtown Guangzhou	July 2006	Rural	3.5	51	11.4	14	17^k	10.7	18^l	1.7	(Lu et al., 2012;Lou et al., 2010)
Yufa, China, 39.5145°N, 116.3055°E, ~40 km south of the Beijing downtown area	August-September 2006	Rural	1.8	71	8.8	5.5	7.2^k	7.0	15^l	2.1	(Lu et al., 2013)
Mexico City, Mexico, 19 °N, 100°W, ~7 km SE of downtown area	March 2006	Urban	4.0	90	49	4.6^e	1.9^e	7.5	31^c	4.1	(Dusanter et al., 2009a;Dusanter et al., 2009b;Molina et al., 2010)
University of Houston (70 m above ground level), USA, 29.7176°N, 95.3413°W, 5 km SE of tall buildings in downtown Houston	August-September 2006	Urban (Tower)	3.1	68	4	15	12.5	5.3	45^d	8.5	(Mao et al., 2010)
University of Houston (70 m above ground level), USA, 29.7176°N, 95.3413°W, 5 km SE of tall buildings in downtown Houston	April-May 2009	Urban (Tower)	-	47	2.5	8.8^e	6.3^e	3	18^j	6	(Ren et al., 2013;Lee et al., 2013)

Location	Date	Type									Reference
Paris, France, 48.718°N, 2.207°E, ~14 km SW of Paris	July 2009	Suburban	2.2	35	4.3	4.2	1.3[m]	0.75[n]	7.1[o]	9.5	(Michoud et al., 2012)
Pasadena, USA, 34.1408°N, 118.1223°W, ~18 km NE of downtown	May-June 2010	Suburban	2.1 (2.5)[p]	45 (72)[p]	19 (9)[p]	3.5 (4.0)[p]	2.0 (5.0)[p]	4.0 (5.3)[p]	33 (23)[p,q]	8.3 (4.3)	(Griffith et al., 2016)
London, England, 51°31'16″N, 0°12'48″W, in central London	July-August 2012	Urban	-	24.2 (37.4)[r]	13.1 (24.3)[r]	2.1 (3.0)[r]	2.0 (0.6)[r]	4.9	5.6[g]	1.1	(Whalley et al., 2018; Whalley, 2016)
Wangdu, China, 38.71°N, 115.15°E, ~35 km SW of Baoding and 170 km SW of Beijing	June-July 2014	Rural	1.8	88	8.2	8.3	7.7	4.8	14.7[b]	3.1	(Tan et al., 2017)
Heshan, China, 22.728°N, 112.929°E, ~6 km SW of the city of Heshan and 50 km SW of Guangzhou and Foshan	October-November 2014	Suburban	1.3	51	26.9	4.8	2.3	5.1	18.1[b]	3.5	(Tan et al., 2019a)
Taizhou, China, 32.56°N, 119.99 °E, ~200 km NW of Shanghai	May-June 2018	Suburban	2.1	82	3.6	10.6	11.4	6.8	11.4[j]	1.7	This study

833 [a] Take from a typical day. [b] Calculated from measured peroxy radical with NO reaction. [c] Calculated from measured HO_2 with NO reaction. [d] Calculated from measured HO_2 with NO. and scaled RO_2
834 (measured HO_2 times the ratio of modelled RO_2 to HO_2) with NO. [e] Median. [f] Median and revised. [g] 11:00-15:00 mean. [h] Calculated by summing all of the reaction rates for NO to NO_2
835 conversions. [i] For smog-free day and smog day (in parenthesis) separately. [j] Calculated from measured HO_2 and modelled RO_2 with NO. [k] HO_2^*(HO_2 and partial RO_2). [l] Calculated from
836 modelled HO_2 and RO_2 with NO. [m] Total peroxy radicals (HO_2+RO_2). [n] 8:00-16:00 mean. [o] Calculated by measured total peroxy radicals (HO_2+RO_2) with NO. [p] For week days and
837 weekend days (in parenthesis) separately. [q] Calculated from measured HO_2^* with NO. [r] For westerly flow and easterly flow (in parenthesis) separately. [s] Calculated by the ratio between
838 $F(O_x)$ and $P(RO_x)$.

839

840
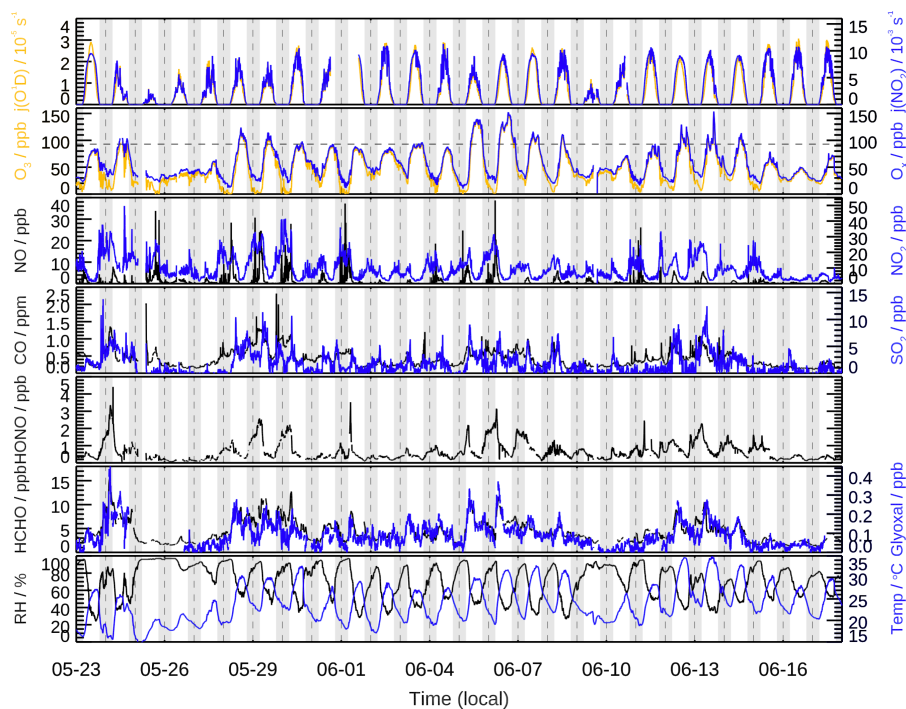
Figure 1. Time series of measured photolysis frequencies ($j(O^1D)$, $j(NO_2)$), relative humidity (RH),

ambient temperature (T), and concentrations of O_3, O_x (=O_3+NO_2), NO, NO_2, CO, SO_2, HONO,

formaldehyde (HCHO), and glyoxal (CHOCHO). The dotted horizontal line represents the Chinese

**national air quality standard level II of O_3 (hourly averaged limit 93 ppb). The grey areas denote**

nighttime.

846

33
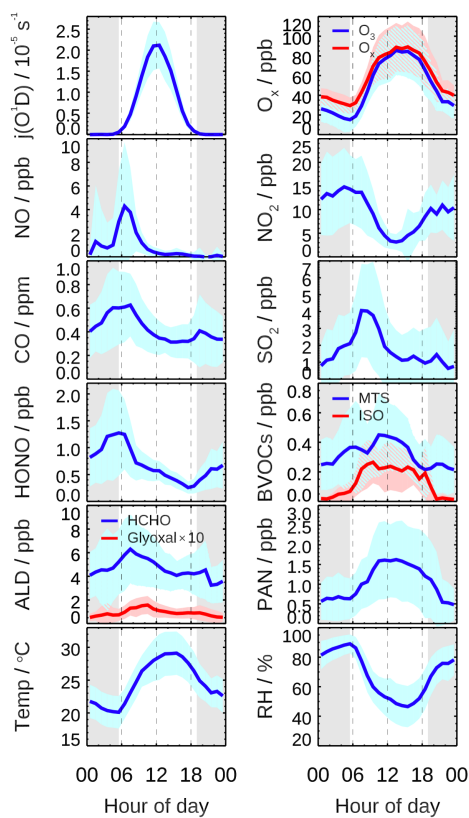
Figure 2. Mean diurnal profiles of measured photolysis frequencies (j(O^{1}D)), relative humidity (RH), ambient temperature (T), and concentrations of O$_3$, O$_x$ (=O$_3$+NO$_2$), NO, NO$_2$, CO, SO$_2$, HONO, formaldehyde (HCHO), glyoxal (CHOCHO), biogenic VOCs (monoterpenes, isoprene), and PAN. Data are averaged over the period with HO$_x$ radical measurement. Colored areas denote the standard deviation of variability (1σ). The grey areas denote nighttime.

859
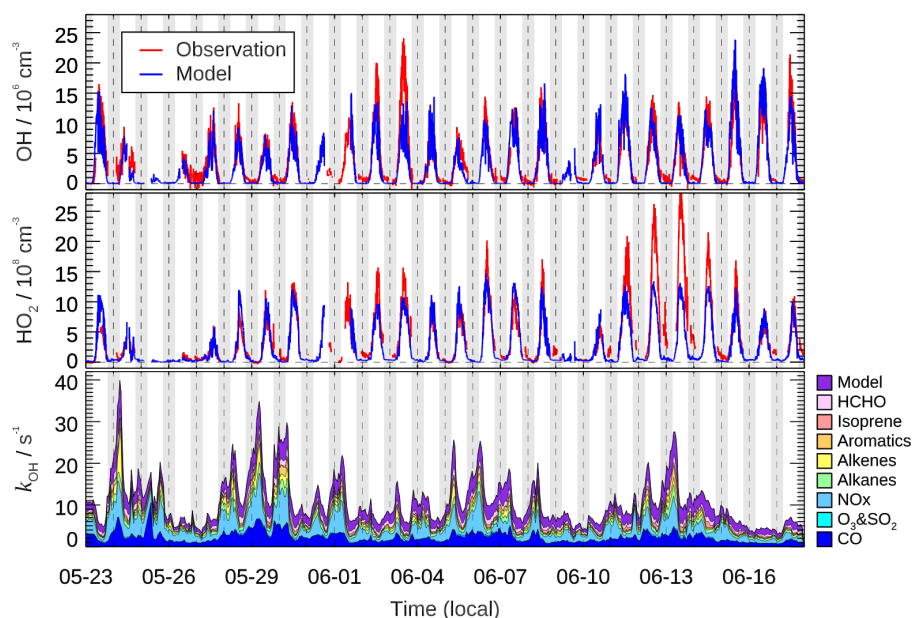
Figure 3. Time series of observed and modelled OH and HO$_2$ concentrations, and the modelled

860

861 **grouped OH reactivity (k_{OH}). Vertical dash lines denote midnight. The grey areas denote nighttime.**

862

863
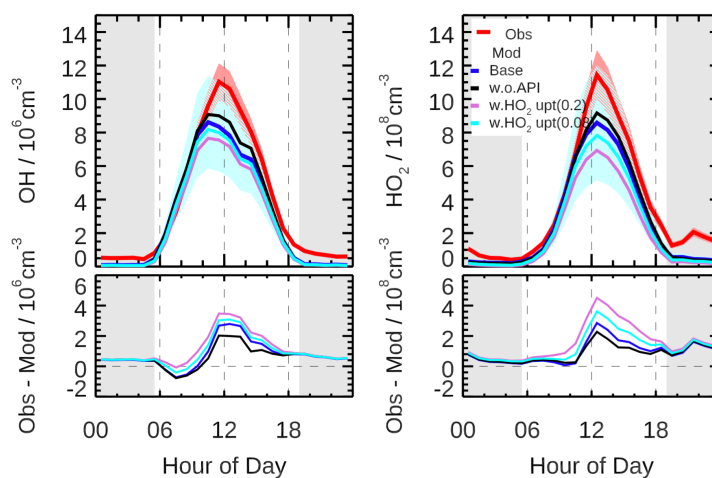
Figure 4. The mean diurnal profiles of measured and modelled OH and HO$_2$ concentrations (upper

864

865 **panel) as well as the discrepancies between observation and model (lower panel) in different scenarios**

866 **(Scenario1: base case; Scenario2: without α-pinene constrained; Scenario 3: with HO$_2$ heterogeneous**

867 **uptake process considered by assuming the uptake coefficient of 0.2; Scenario 4: with HO$_2$**

868 **heterogeneous uptake process considered by assuming the uptake coefficient of 0.08). Colored areas**

869 **denote 1σ uncertainties of measured (red) and base case modelled (blue) radical concentrations,**

870 **respectively. The grey areas denote nighttime.**
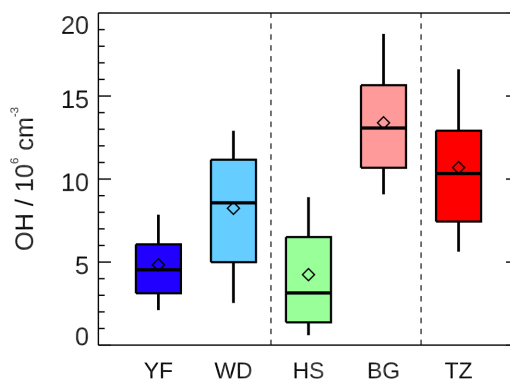
871

872 **Figure 5. Summary of OH radical concentrations (noon time, 11:00-13:00) measured in five summer**

873 **field campaigns in China. Yufa (YF) and Wangdu (WD) campaign in North China Plain, Heshan (HS)**

874 **and Backgarden (BG) campaign in Pearl River Delta, and Taizhou (TZ, this study) campaign in**

875 **Yangtze River Delta. The box-whisker plot shows the 90th, 75th, 50th, 25th, and 10th percentile values of**

876 **noon OH radical concentrations in each campaign. The diamond shows the mean values of noon OH**

877 **radical concentrations.**

878

879
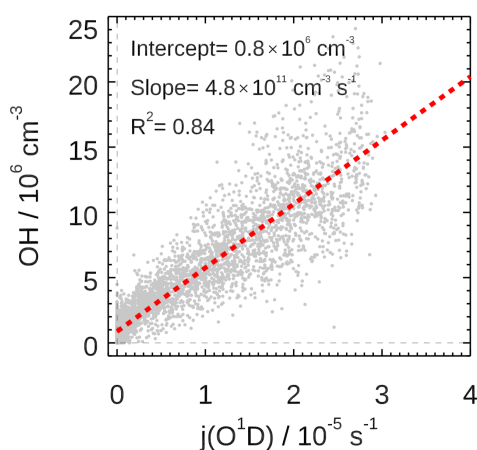
Figure 6. Correlation between measured OH and j(O¹D). Grey scatter plot represents the 5 min observation result for the EXPLORE-YRD campaign. A linear fit which takes both measurements error into account is applied. The linear fit lines and correlation slopes, intercept and coefficients are also shown.

884

885

886
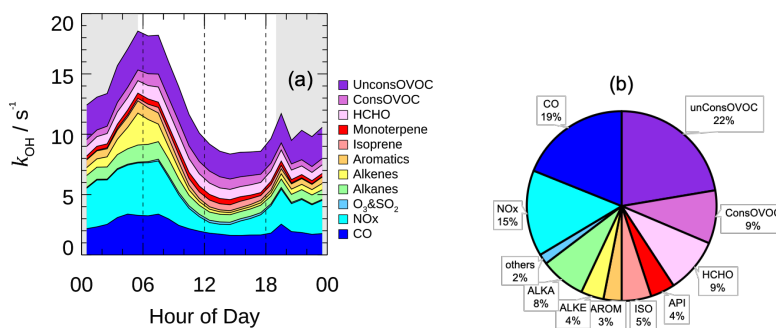
Figure 7. (a) The mean diurnal profiles of speciated OH reactivity. The grey areas denote nighttime. (b) Breakdown of modelled OH reactivity for daytime conditions (08:00-16:00).

889
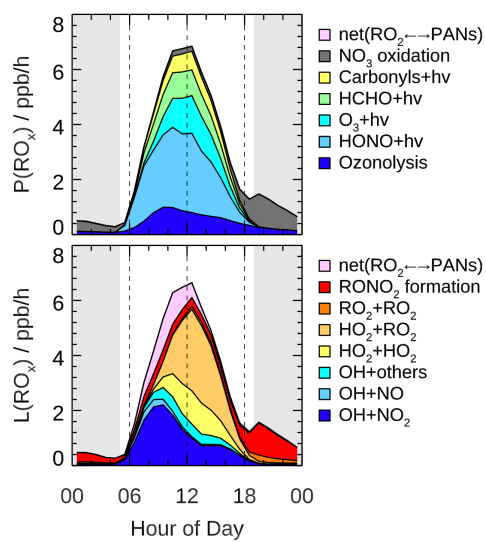
Figure 8. Hourly mean diurnal profiles of primary sources and sinks of RO_x radicals from model calculations. The grey areas denote nighttime.

895
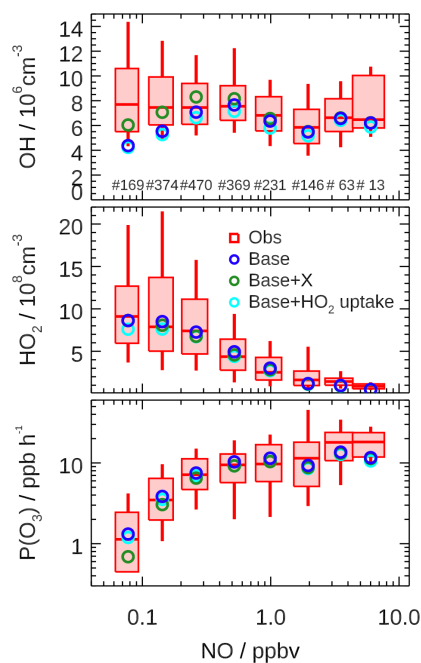
**Figure 9. Dependence of measured and modelled OH, HO$_2$, and P(O$_x$) on NO concentrations for daytime condition (j(O^{1}D)> 0.5×10^{-5} s^{-1}). Box-whisker plot shows the median, the 75 and 25 percentiles, and the 90 and 10 percentiles of the measured results for each NO interval bins. Only median values are shown for modelled results. Numbers in upper panel represent the data points incorporated in each NO interval. Results from base case, with additional recycling process by a species X (equivalent to 100 ppt NO), and with additional HO$_2$ heterogeneous uptake process (γ assuming of 0.08) are all plotted.**

903

904
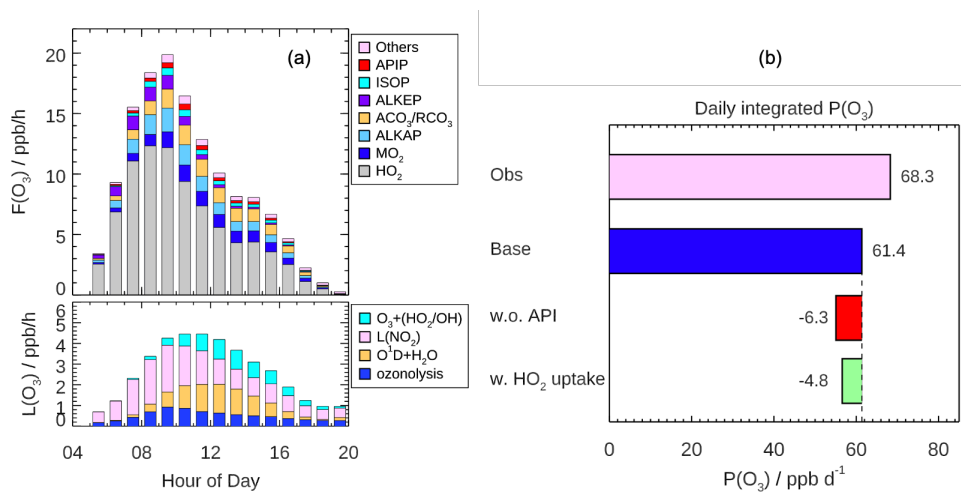
Figure 10. (a) Mean diurnal profiles of the speciation ozone formation rate ($F(O_x)$) from different peroxy radical species (upper panel) and the speciation ozone destruction rate ($L(O_x)$, lower panel) calculated based on the measured OH and HO_2 and modelled RO_2 radicals. (b) Daily (08:00-16:00) integrated net ozone production calculated from the observed and modelled radical concentration, respectively. The discrepancies between two model scenarios run (Scenario1: without α-pinene constrained; Scenario2: with HO_2 heterogeneous uptake considered by assuming γ of 0.08) from base case are also shown.